

A high-order finite volume method on unstructured grids using RBF reconstruction



Yilang Liu^a, Weiwei Zhang^{a,*}, Yuewen Jiang^b, Zhengyin Ye^a

^a School of Aeronautics, Northwestern Polytechnical University, No. 127 Youyi West Road, Xi'an 710072, China

^b Department of Engineering Science, University of Oxford, Oxford, OX1 3PJ, UK

ARTICLE INFO

Article history:

Received 27 January 2016

Received in revised form 29 May 2016

Accepted 19 June 2016

Available online 18 July 2016

Keywords:

Finite volume method

Unstructured grids

High order scheme

RBF reconstruction method

Navier–Stokes equations

ABSTRACT

This paper proposes a high-order finite volume method based on radial basis function (RBF) reconstruction for the solution of Euler and Navier–Stokes equations on unstructured grids. Unlike traditional polynomial K-exact method, RBF method has stronger adaptability for different reconstruction stencils and more flexibility in choosing interpolating points. We expatiate on the detailed process of flow-field reconstruction by using multiquadric (MQ) basis function for the second-order and third-order schemes on unstructured triangular grids. Subsequently, we validate the accuracy order of RBF method through the numerical test case. Furthermore, the method is used to solve several typical flow fields. Compared with traditional K-exact high-order scheme, RBF method is more accurate and has lower numerical dissipation, which can obtain more elaborate and precise results.

© 2016 Elsevier Ltd. All rights reserved.

1. Introduction

Researchers of computational fluid dynamics (CFD) have kept pursuing the accuracy of numerical simulation and the adaptability to complex configurations. Although finite difference method for high-order scheme performs well and has been successfully used in flow-field numerical simulation, it mainly implement on structured grids [1,2]. Unstructured grids have random data storage, disordered adjacent grid nodes and controllable distribution of elements and nodes. So, they have a natural ability to adapt to complex shapes and can easily control grid distribution to achieve adaptive meshes. Thus, it is significant to develop high order numerical scheme on unstructured grids for both fundamental theory research and practical engineering applications. Although the second-order accuracy schemes have played an important role in aircraft design and application, they still have large numerical dissipation and dispersion. For some complex flow problems, such as wave propagation, vortex-dominated flows including high-lift configuration, helicopter blade vortex interaction, as well as large eddy simulation and direct numerical simulation of turbulence, high-order accuracy schemes must be used to obtain more elaborate and detailed results [3]. Furthermore, as pointed out by Jameson [4], the use of second-order finite volume methods cannot, on realistic meshes, reliably predict complex separated, unsteady and vortex dominated flows, and future research should focus on high-order methods with minimal numerical dissipation for unstructured meshes. However, the development of higher-order finite volume method on unstructured grids is technically difficult [5,6].

The key issue of solving flow equations by finite volume method is to reconstruct the distribution of unknown variables at the interface of the control volumes using the cell averaged state variables. For the second-order scheme, one of the most widely used reconstruction methods is based on the Taylor series expansion first proposed by Barth [7,8]. This method

* Corresponding author.

E-mail address: aeroelastic@nwpu.edu.cn (W. Zhang).

assumes that the solution is piecewise linearly distributed over the control volume. It implements a Taylor-series around the neighboring center of grid faces where only the linear term is retained, and then solves the equations by the least-squares approach to obtain the cell center gradient and values at the interface. Frink [9] proposed a simpler linear vertex reconstruction method that did not require explicit evaluation of the center grid variable gradient. Additionally, the gradient at the cell center can be approximated by a simple finite difference after determining the nodal values by inverse distance weighing. The above two methods belong to polynomial flow-field reconstruction method. Barth and Frederickson [10] extend it to high-order finite volume schemes, namely K-exact least-squares reconstruction method, which has been widely applied in computational dynamics [5,6,11–16].

Traditional polynomial reconstruction method is a kind of global fitting method, and the expanded item of Taylor polynomial strictly matches the accuracy order of interpolation method. Fewer interpolation points result in lower numerical accuracy, whereas more interpolation points result in over-fitting, especially for high-order finite volume method on unstructured grids. Unlike polynomial reconstruction method, Lancaster and Salkauskas [17] proposed a moving least-squares (MLS) method which is mainly used in curve and surface fittings. Afterward, CFD researchers successfully introduced it into solving flow-field governing equations [18–20]. MLS method is a local fitting method in which each interpolation base point corresponds with a polynomial shape function and a weight function. It is very convenient to use this method to control the fitting accuracy and smoothness by changing the degrees of shape functions and weight functions. This method has been thoroughly studied by Cueto-Felgueroso [18–20]. Moving Kriging (MK) method, which was first proposed by Gu [21], is also a candidate interpolation technique for flow-field reconstruction. Gu successfully constructed the shape function with MK interpolation instead of MLS and applied it to element-free Galerkin method for solving the weak form of the boundary value problem. Subsequently, the method was widely used in solid mechanic problems [22–25]. Chassaing [26] first introduced the MK interpolation in high-order finite volume method. The successive derivatives of the flow variables in each cell are deduced from the interpolation function, and MK-FV method is proved to be an interesting alternative for the development of high-order methodology for complex geometries. Radial basis function (RBF) interpolation method [27], because of its excellent performance of scattered data fitting and brief mathematical expression, has been widely used in many different domains, such as mesh deformation [28,29], nonlinear aerodynamic modeling [30,31], and partial differential equations solving [32–34]. Sonar [35,36] first applied the RBF interpolation method to finite volume scheme of ENO-type using the thin splines base function. In terms of solving partial differential equations, partial derivatives of equations can be approximately expressed by the linear combination of RBFs, proposed by C. Shu [37], which can be used for numerical solution by finite difference method.

This paper introduces RBF interpolation in flow-field reconstruction for high-order finite volume scheme on unstructured grids. We expatiate on the detailed process of achieving cell-centered high-order scheme for finite volume method by using MQ basis function. It is implemented in terms of three main aspects: the reconstruction of the flow variables at control volume interfaces, the selection of the reconstruction stencil and the treatment of the curved boundary condition. Above this, the accuracy order of RBF reconstruction method is validated through numerical test cases. Furthermore, the method is used to solve several inviscid and viscous typical flow fields, and meanwhile, the computed results are compared with the results from traditional polynomial reconstruction methods.

The outline of this paper is organized as follows. Section 2 briefly describes the finite volume formulation of the governing equations. The high-order discretization algorithm based on RBF reconstruction is detailed in Section 3. Section 4 presents a comprehensive assessment of the scheme by several numerical experiments for inviscid and viscous flows and the concluding remarks are drawn in Section 5.

2. Governing equations and high-order finite volume formulation

The integral form of two-dimensional Navier–Stocks equations can be written as:

$$\frac{\partial}{\partial t} \iint_{\Omega} \mathbf{Q} d\Omega + \oint_{\partial\Omega} \mathbf{F}(\mathbf{Q}) \cdot \mathbf{n} d\Gamma = \oint_{\partial\Omega} \mathbf{G}(\mathbf{Q}) \cdot \mathbf{n} d\Gamma \quad (1)$$

where Ω is the control volume; $\partial\Omega$ is the boundary of control volume; and $\mathbf{n} = (n_x, n_y)^T$ denotes the outer normal vector of the control volume boundary. The vector of conservative variables \mathbf{Q} , inviscid fluxes $\mathbf{F}(\mathbf{Q}) = (\mathbf{F}_x(\mathbf{Q}), \mathbf{F}_y(\mathbf{Q}))$ and viscous fluxes $\mathbf{G}(\mathbf{Q}) = (\mathbf{G}_x(\mathbf{Q}), \mathbf{G}_y(\mathbf{Q}))$ are given by the following equations:

$$\mathbf{Q} = \begin{Bmatrix} \rho \\ \rho u \\ \rho v \\ E \end{Bmatrix} \quad \mathbf{F}_x(\mathbf{Q}) = \begin{Bmatrix} \rho u \\ \rho u^2 + p \\ \rho uv \\ u(E + p) \end{Bmatrix} \quad \mathbf{F}_y(\mathbf{Q}) = \begin{Bmatrix} \rho v \\ \rho uv \\ \rho v^2 + p \\ v(E + p) \end{Bmatrix}$$

$$\mathbf{G}_x(\mathbf{Q}) = \mu \begin{Bmatrix} 0 \\ 2u_x - \frac{2}{3}(u_x + v_y) \\ v_x + u_y \\ u \left(2u_x - \frac{2}{3}(u_x + v_y) \right) + v(v_x + u_y) + \frac{T_x}{(\gamma - 1)\Pr} \end{Bmatrix}$$

$$\mathbf{G}_y(\mathbf{Q}) = \mu \left\{ + \begin{array}{l} 0 \\ v_x + u_y \\ 2v_y - \frac{2}{3}(u_x + v_y) \\ u(v_x + u_y) + v \left(2v_y - \frac{2}{3}(u_x + v_y) \right) + \frac{T_y}{(\gamma - 1) \text{Pr}} \end{array} \right\}$$

where ρ denotes density; u and v are the x and y direction components of the velocity vector; p is the pressure; E is the total energy per unit volume; μ is the dynamic molecular viscosity; T is the temperature; Pr is the Prandtl number; and γ is the ratio of specific heats. For the ideal gas γ is equal to 1.4. According to Sutherland's law, the dynamic viscosity is given by

$$\mu = \mu_{\text{ref}} \frac{T_{\text{ref}} + S_0}{T + S_0} \left(\frac{T}{T_{\text{ref}}} \right)^{\frac{3}{2}} \quad (2)$$

where T_{ref} and μ_{ref} are physical constants of reference temperature and viscosity, and S_0 is the Sutherland temperature. The values of them are $T_{\text{ref}} = 273.15$ K, $\mu_{\text{ref}} = 1.716 \times 10^{-5}$ kg/(m s) and $S_0 = 110$ K, respectively. The equations of state for the ideal gas is

$$p = (\gamma - 1) \left[E - \frac{\rho}{2} (u^2 + v^2) \right]. \quad (3)$$

In the cell-centered finite volume method, the computational domain is divided into non-overlapping control volumes that completely cover the domain. The interface variables are derived from the average values of the grid cells to calculate the fluxes of control volumes. Through spatial discretization, the equations of the integral form are translated to ordinary differential equations in time, and the flow variables are obtained by the time marching method. The semi-discrete finite-volume formulation of the flow equations is

$$\frac{d\bar{\mathbf{Q}}_i}{dt} = -\frac{1}{|\Omega_i|} \sum_{m \in N(i)} \sum_{j=1}^q |\Gamma_{i,m}| \omega_j (\mathbf{F}(\mathbf{Q}(x_j, y_j)) - \mathbf{G}(\mathbf{Q}(x_j, y_j))) \cdot \mathbf{n}_{i,m} \quad (4)$$

where $|\Omega_i|$ denotes the volume of the cell i ; $N(i)$ is the set of cells neighboring cell i ; and $\Gamma_{i,m}$ is the interface area between cell i and the neighbor. q and ω_j denote the Gauss integral points and the weight coefficients of the interface, respectively; and $\mathbf{n}_{i,m}$ is the outer normal vector of the interface. The cell averaged value of the control volume i is $\bar{\mathbf{Q}}_i$, which is given by

$$\bar{\mathbf{Q}}_i = \frac{1}{|\Omega_i|} \int_{\Omega_i} \mathbf{Q}(x, y) d\Omega. \quad (5)$$

Here, we must clarify that the cell averaged value $\bar{\mathbf{Q}}_i$ is different from the cell centroid value. For the second-order scheme, the two values can be simply considered equal to each other; while for the high-order scheme, it will introduce a second-order error in the solution reconstruction by using the cell centroid value to represent the cell averaged value. If neglecting this key point, the scheme will only achieve the second-order accuracy.

The numerical fluxes at the right hand of Eq. (4) can be evaluated by upwind schemes. According to the Godunov-type method, the interface normal fluxes are calculated by Riemann solver:

$$\mathbf{F}(\mathbf{Q}_{i,m}) \cdot \mathbf{n}_{i,m} \approx \tilde{\mathbf{F}}(\mathbf{Q}_{i,m}^L, \mathbf{Q}_{i,m}^R, \mathbf{n}_{i,m}) \quad (6)$$

where the superscripts “ L ” and “ R ” denote the states of flow variables approaching to the left and right sides of the cell interface, respectively. This paper adopts Roe [38] scheme to compute the numerical fluxes, where $\mathbf{Q}_{i,m}^L$ and $\mathbf{Q}_{i,m}^R$ are used to evaluate Roe's average state. In order to evaluate the numerical fluxes, the middle point of each interface is used in the second-order accuracy method, and two Gauss points are used in the third-order method.

The semi-discrete formulation of flow Eq. (4) can be translated to ordinary differential equations in time after obtaining the discrete numerical fluxes:

$$\frac{d\bar{\mathbf{Q}}_i}{dt} = \bar{R}_i \quad (7)$$

where \bar{R}_i denotes the sum of inviscid and viscous fluxes. Finally, the semi-discrete system (7) is marched in time using an explicit four-stage four-order Runge–Kutta scheme:

$$\begin{aligned} \bar{Q}_i^{(0)} &= \bar{Q}_i^n \\ \bar{Q}_i^{(1)} &= \bar{Q}_i^{(0)} + \alpha_1 \Delta t \bar{R}_i^{(0)} \\ \bar{Q}_i^{(2)} &= \bar{Q}_i^{(0)} + \alpha_2 \Delta t \bar{R}_i^{(1)} \end{aligned}$$

$$\begin{aligned}\bar{Q}_i^{(3)} &= \bar{Q}_i^{(0)} + \alpha_3 \Delta t \bar{R}_i^{(2)} \\ \bar{Q}_i^{(4)} &= \bar{Q}_i^{(0)} + \alpha_4 \Delta t \bar{R}_i^{(3)} \\ \bar{Q}_i^{(n+1)} &= \bar{Q}_i^{(4)}\end{aligned}\quad (8)$$

where the constant values are $\alpha_1 = \frac{1}{4}$, $\alpha_2 = \frac{1}{3}$, $\alpha_3 = \frac{1}{2}$, $\alpha_4 = 1$. For the steady problems, local time step can be employed in convergence acceleration.

3. Reconstruction method based on RBF

In order to calculate numerical fluxes, the flow-field variables at the interface of the control volumes should be first obtained by using the given cell averaged variables, which are directly related to the accuracy of the entire flow-field numerical solution. In this paper, the RBF interpolation method is used to reconstruct the flow field. For the traditional polynomial reconstruction method, the expanded item of Taylor polynomial strictly matches the accuracy order, which is determined by the number of stencil grids. That is, we must have 3, 6 and 10 cells in 2D and 4, 10 and 20 cells in 3D for the construction of a linear, quadratic and cubic polynomial, respectively. For example, if we want to construct a third-order scheme in 3D case by polynomial method, while only 9 or fewer cells are contained on some stencils at most which approach to but are just fewer than 10, then the accuracy fails to achieve third order on these stencils and must reduce to the second-order accuracy by applying the least squares method to obtain compromise results. Thus, it may cause accuracy mutation or over-fitting in local region, especially for higher-order or higher dimensions cases. However, RBF method has strong adaptability for different reconstruction stencils, and it has no influence on the structure of interpolation expression as the number of stencil grids increases or decreases. So the numerical accuracy order will preserve a continuous change instead of mutation.

3.1. Process of RBF reconstruction method

The general form of RBF can be written as:

$$\mathbf{y}(\mathbf{r}) = \sum_{i=1}^N \omega_i \varphi (\|\mathbf{r} - \mathbf{r}_i\|) \quad (9)$$

where $\mathbf{y}(\mathbf{r})$ is the interpolation function; $\varphi (\|\mathbf{r} - \mathbf{r}_i\|)$ denotes RBF, and the subscript i denotes each cell in reconstruction stencil; N is the sum of basis functions; $\|\mathbf{r} - \mathbf{r}_i\|$ is the distance between the vector \mathbf{r} and the vector \mathbf{r}_i ; and ω_i is the weight coefficient of each RBF.

For the reconstruction stencil $S = \{V_1, V_2, \dots, V_N\}$, the incremental primitive variables are chosen to reconstruct the value distribution of the center cell m . The incremental variables $\Delta \bar{\mathbf{q}}$ are defined as the difference between the mean values of the center cell $\bar{\mathbf{q}}_m$ and the mean values of each grid $\bar{\mathbf{q}}_i$ of the reconstruction stencil:

$$\begin{aligned}\Delta \bar{\mathbf{q}} &= \bar{\mathbf{q}}_i - \bar{\mathbf{q}}_m \quad (i = 1, 2, \dots, N) \\ \bar{\mathbf{q}} &= \{\bar{\rho}, \bar{u}, \bar{v}, \bar{p}\}.\end{aligned}\quad (10)$$

The RBF of each reconstruction stencil can be expressed by $\mathbf{y}(\mathbf{r}) = \sum_{i=1}^N \omega_i \varphi (\|\mathbf{r} - \mathbf{r}_i\|)$, and the conservation of the mean property requires the following equation:

$$\frac{1}{|\Omega_i|} \int_{\Omega_i} \mathbf{y}(\mathbf{r}) d\Omega = \Delta \bar{\mathbf{q}}_i. \quad (11)$$

Taking the RBF expression (9) into the above equation we can obtain:

$$\frac{1}{\Omega_i} \sum_{i=1}^N \int_{\Omega_i} \omega_i \varphi (\|\mathbf{r} - \mathbf{r}_i\|) d\Omega = \Delta \bar{\mathbf{q}}_i \quad (12)$$

where $\mathbf{r}_i = (x_i, y_i)$ is the reference point of RBF, which can be chosen as the arbitrary point in space region in principle; and for the convenience of calculation, we recommend the usual choice which is the centroid of control volume. According to Eq. (12), a system of linear algebraic equations can be obtained in each reconstruction stencil

$$\Phi \boldsymbol{\omega} = \Delta \bar{\mathbf{q}}. \quad (13)$$

The reconstruction matrix Φ and the weight coefficients $\boldsymbol{\omega}$ are defined as below:

$$\Phi = \begin{bmatrix} \varphi_{11} & \varphi_{12} & \cdots & \varphi_{1N} \\ \varphi_{21} & \varphi_{22} & \cdots & \varphi_{2N} \\ \vdots & \vdots & \ddots & \vdots \\ \varphi_{N1} & \varphi_{N2} & \cdots & \varphi_{NN} \end{bmatrix}$$

$$\varphi_{ij} = \frac{1}{|\Omega_i|} \int_{\Omega_i} \varphi(\|\mathbf{r} - \mathbf{r}_j\|) d\Omega \quad (i, j = 1, 2, \dots, N) \quad (14)$$

$$\boldsymbol{\omega} = [\omega_1, \omega_2, \dots, \omega_N]^T$$

where $\mathbf{r}_j = (x_j, y_j)$ is the reference point of RBF for the cell j . φ_{ij} in Eq. (14) is the surface integral in control volume i by each RBF. Considering that the matrix Φ in Eq. (13) is only related to the geometric property of the control volume, for the steady cases or unsteady cases without grid deformation, Φ remains unchanged. Therefore, we can compute and prestore the reconstruction matrix Φ as a preprocessing step, which can significantly reduce the computational time. However, storing the matrix Φ for every cell requires more computer memory. As to the two-dimensional triangular grids, we choose four Gauss integral points to calculate the surface integral φ_{ij} for the third-order scheme. Thus, Eq. (14) can also be expressed as:

$$\varphi_{ij} = \frac{1}{\Omega_i} \sum_{GS=1}^4 \lambda_{GS} \varphi(\|\mathbf{r}_{i,GS} - \mathbf{r}_j\|) \quad (i, j = 1, 2, \dots, N) \quad (15)$$

where GS denotes Gauss integral point, and λ_{GS} is the coefficients of Gauss integral, and $\|\mathbf{r} - \mathbf{r}_j\|$ denotes Euclidean distance:

$$\|\mathbf{r} - \mathbf{r}_j\| = \sqrt{(x - x_j)^2 + (y - y_j)^2}.$$

The weight coefficients $\boldsymbol{\omega}$ of each cell can be obtained by solving Eq. (13), and then we can determine the distribution of incremental values of the reconstruction stencil by substituting $\boldsymbol{\omega}$ into Eq. (9). Finally, the mean values of the center cell $\bar{\mathbf{q}}_i$ are added to incremental values $\Delta\mathbf{q}_{i,m}$, and the final interface variables $\mathbf{q}_{i,m}$ are given by

$$\mathbf{q}_{i,m} = \bar{\mathbf{q}}_i + \Delta\mathbf{q}_{i,m} = \bar{\mathbf{q}}_i + \sum_{i=1}^{N(i)} \omega_i \varphi(\|\mathbf{r}_{i,m} - \mathbf{r}_j\|). \quad (16)$$

After obtaining the interface variables of the left and the right state, the inviscid fluxes can be easily computed by Roe's scheme.

In order to evaluate the viscous fluxes, the remaining task is the computation of the gradients of the velocity and temperature at the interface of the control volumes. There are two ways to accomplish it. One is to define an auxiliary control volume centered at the interface and to employ the Green–Gauss theorem, where the auxiliary control volume is constructed by using two adjacent cell centroids and the endpoints of their common edge. So we can compute the interface gradients of variables at the edge-midpoint. The other way to compute the gradients at the interface is to use the average of the reconstructed gradients on either side of the control volume face at the Gauss points. Since we have already computed the distribution of flow variables inside each control volume, the gradients of the left state at the interface can be easily obtained by derivation from Eq. (9)

$$\nabla q_{i,m}^L = \sum_{i=1}^N \omega_i \cdot \nabla \varphi(\|\mathbf{r}_{i,m} - \mathbf{r}_i\|). \quad (17)$$

The gradients of Gauss points at the interface can be evaluated by the simple average of both sides:

$$\nabla q_{i,m} = \frac{1}{2} (\nabla q_{i,m}^L + \nabla q_{i,m}^R). \quad (18)$$

The gradients computed by Green–Gauss theorem of the first approach can only achieve the first-order accuracy, while the gradients of the latter approach are the second-order accuracy. However, the method of Green–Gauss theorem is better than the one of the average of gradients in numerical stability.

RBF interpolation method has high precision and strong flexibility. Different kinds of basis functions or different shape parameters of the same RBF are likely to generate different results [33,39]. MQ basis function, which was first proposed by Hardy [27], performs better in precision than other RBFs and it has been widely used in application. Therefore, in this paper, we will concentrate on MQ basis function, and other RBFs can be implemented in the same manner. The expression of the MQ basis function is:

$$\varphi(\mathbf{r}) = \sqrt{c + \mathbf{r}^2} \quad (19)$$

where c is the shape parameter, the value of which can influence both the accuracy of RBF interpolation and the numerical stability [40,41]. To determine the optimal value of the shape parameter c , there is not a consensual criterion, and the optimal c may differ in different problems [34]. We propose to set the shape parameter c to 10, experimentally. Because of the different mesh scales of spatial discretization, the far field mesh scale is several hundred times larger than the wall boundary's. This situation exists especially in viscous meshes with the boundary layer. Therefore, the shape parameter c and the Euclidean distance \mathbf{r} in Eq. (19) should be normalized for non-uniform meshes. We choose the local scale Δ_{avg} as the reference distance, which is defined by the average distance of the central cell and other cells in the reconstruction stencil. The MQ basis function after normalization is:

$$\varphi(\mathbf{r}) = \sqrt{\frac{c}{\Delta_{avg}}} + (\mathbf{r}/\Delta_{avg})^2. \quad (20)$$

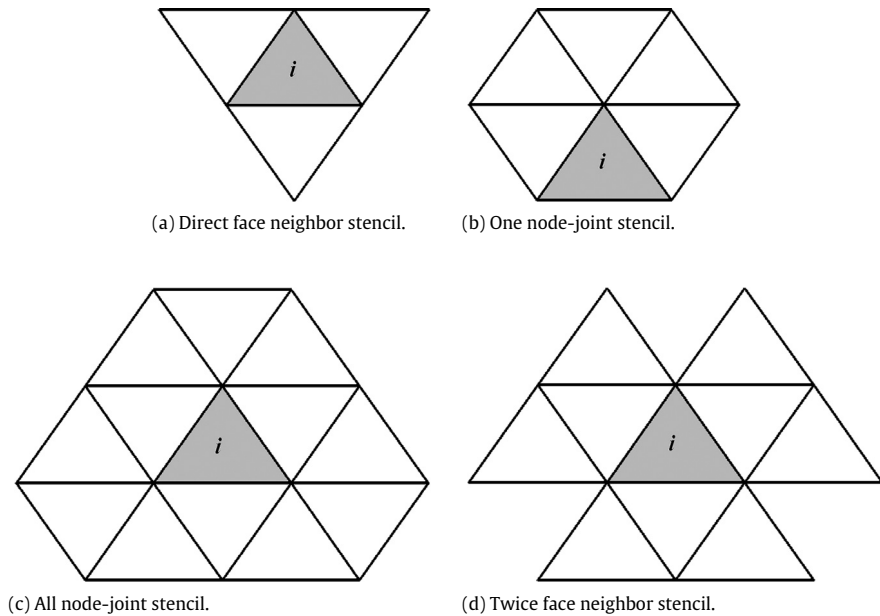


Fig. 1. Four different kinds of reconstruction stencils.

3.2. Reconstruction stencil

In the cell-centered finite volume method, each grid cell has only one degree of freedom to represent the mean value of the flow variables. Thus, it needs to expand grid stencil to reconstruct the high-order distribution of the flow variables. It is particularly important to select the grid stencil for the accuracy of flow-field numerical solution. Due to the random spatial distribution of unstructured grids, it provides more flexibility to choose the reconstruction stencil. On the whole, we recommend two basic principles for stencil selection. To begin with, the reconstruction stencil should be compact, that is, the cells in the stencil should not be topologically far from the center control volume. Secondly, the sum of grid cells of the stencil should compromise computational cost and solution accuracy. On the one hand, the number of cells should at least satisfy the requirement of numerical accuracy; and on the other hand, the cells should not be too many to reduce the calculation efficiency. We offer four kinds of reconstruction stencils as shown in Fig. 1.

Fig. 1(a) is the direct face neighbor stencil which shares the same edge of the center cell. Fig. 1(b) is the one node-joint stencil that shares one node opposite to the edge of the center cell. Fig. 1(c) is the all node-joint stencil that shares all the nodes of center cell. Fig. 1(d) is the twice face neighbor stencil which expands face neighbors again the same way as the direct face neighbor stencil. For the reconstruction stencil (a), (c) and (d), the distribution of grids is compact and has good spatial centricity, which will achieve high accuracy and low dissipation. For the second stencil (b), the process of reconstruction corresponds with extrapolation; thus, it will reduce calculation precision while this stencil may have good numerical stability because of the geometry upwind distribution of the grids. Moreover, with regard to the stencil (b) and (c), the sum of cells is relatively suitable for two-dimensional cases, but for three-dimensional problems, it will increase substantially, especially in the region of poor mesh quality. However, for the stencil (a) and (d), the sum of cells is appropriate and easy to control both in two-dimensional and three-dimensional cases. Based on the above analyses, the first stencil is adopted for the second-order reconstruction, and the fourth stencil for third-order reconstruction.

3.3. Treatment of curved boundary condition

One of the most challenging aspects to achieve high-order accuracy is the proper treatment of curved boundaries [6,42]. Ollivier-Gooch has done some excellent research on curved boundary for high order finite volume method, and illustrated when the boundaries are properly treated, it will produce dramatically better results compared with straight boundaries [6]. Moreover, the discontinuous Galerkin method (DGM) is much more sensitive to the treatment of boundaries, and huge errors and wrong solutions may be caused if the straight boundary conditions are used instead of the curved ones [43,44].

For the cell i on the boundary, the reconstruction stencil of the third-order scheme is shown in Fig. 2. Despite the lack of some grids on the boundary, the reconstruction stencil still satisfies the requirement of the third-order accuracy. In this paper, we propose to adopt curved boundary conditions developed by Krivodonova and Berger [43]. In numerical simulation of CFD, the computational boundary does not always coincide exactly with the physical one; and to be more accurate, the “wall tangency” condition refers to the physical boundary not the computational boundary shown in Fig. 3. That is, the

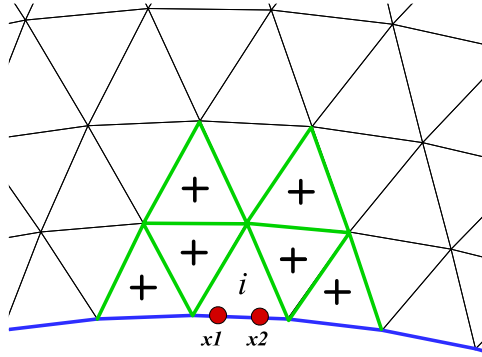


Fig. 2. The reconstruction stencil on boundary of cell i .

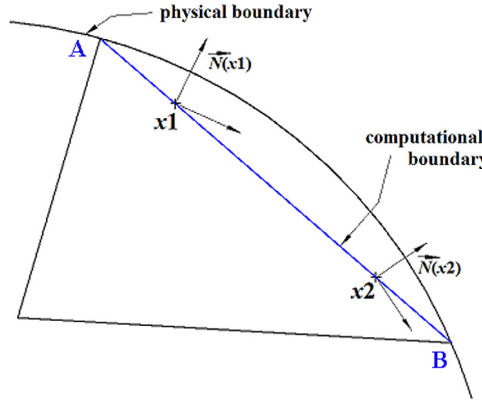


Fig. 3. Curved boundary conditions for the two Gauss points. The unit vectors $\vec{N}(x_1)$ and $\vec{N}(x_2)$ are normal to the physical boundary.

velocity vector must be tangent to the physical surface for inviscid flows, and we express this in the equations below:

$$\vec{v}(\mathbf{x}) \cdot \vec{N}(\mathbf{x}) = 0, \quad \mathbf{x} \in \partial\Omega_j \quad (21)$$

where $\vec{N}(\mathbf{x})$ is the unit normal to the physical geometry at point \mathbf{x} , and $\partial\Omega_j$ is the numerical boundary.

Therefore, the key issue for the curved boundary condition is to calculate the normal vector $\vec{N}(\mathbf{x})$ at the integration points from the available data. According to Krivodonova's method, the physical geometry can be approximated by an arc of the circle passing through the two end points A and B. The radius of the circle is taken to be the average of the radii of two circles passing through three points: points A, B and the point lying on the numerical boundary immediately to the point A or the point B. The vector $\vec{N}(\mathbf{x})$ is perpendicular to the line through the vertex \mathbf{x} and the center of the arc. For boundary cells, the ghost state primitive variables of Gauss points $\mathbf{q}_g = (\rho_g, u_g, v_g, p_g)$ are given by

$$\begin{aligned} \rho_g &= \rho \\ u_g &= u[(N_2)^2 - (N_1)^2] - 2N_1N_2v \\ v_g &= v[(N_1)^2 - (N_2)^2] - 2N_1N_2u \\ p_g &= p \end{aligned} \quad (22)$$

where ρ , u , v and p denote the interior state reconstructed at Gauss points, and N_1, N_2 are the x and y direction components of the unit normal vector to the physical boundary. Once the ghost state values are determined at Gauss points, numerical fluxes are computed as usual interior elements. This approach is very effective and simple to implement. There is no need to compute the location and weight of Gauss points on physical boundary but to modify the velocity normal vector on numerical boundary.

4. Numerical examples

4.1. Non-linear system of Euler equations

Although RBF method has been highly successfully used in practical applications including linear as well as nonlinear, steady state as well as transient problems, there is no strict theoretical foundation for error estimate [45]. We simply

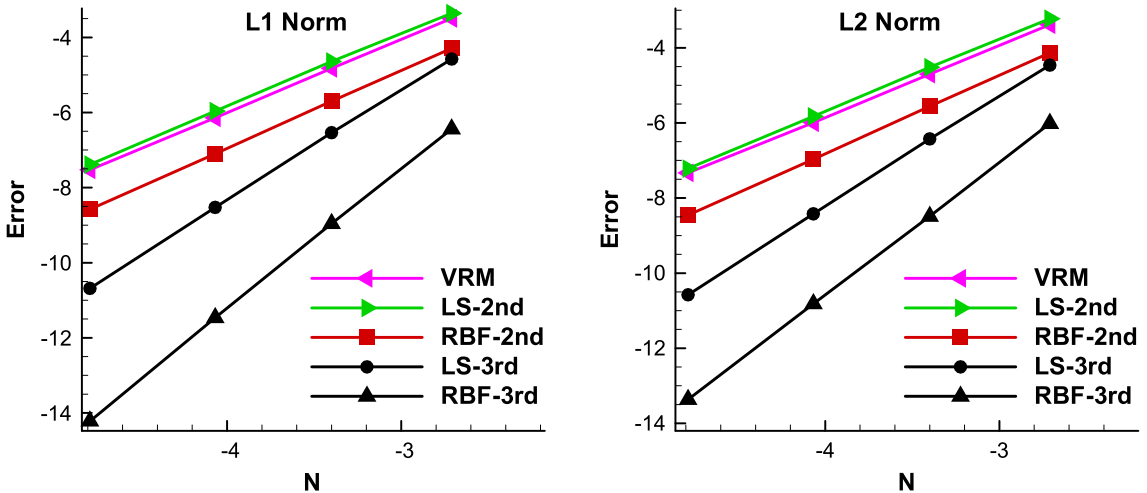


Fig. 4. L_1 and L_2 norm errors of density by different methods for non-linear Euler equations.

prove the accuracy of RBF interpolation method in theory using MQ basis function in one-dimensional problem given in the [Appendix](#).

In the following, we shall conduct numerical experiments to examine the accuracy order of RBF reconstruction method. Firstly we solve the non-linear system of Euler equations [46] on unstructured meshes. The initial conditions of two-dimensional Euler equations are set as below:

$$\begin{cases} u(x, y, 0) = 0.7 \\ v(x, y, 0) = 0.3 \\ \rho(x, y, 0) = 1 + 0.2 \sin(\pi(x + y)) \\ p(x, y, 0) = 1. \end{cases} \quad (23)$$

The computational domain is a square of $(x, y) \in [0, 2] \times [0, 2]$, which is a series of four quasi-uniform triangular meshes that are generated in the domain, ranging in size of $2/10, 2/20, 2/40$ and $2/80$. Both directions are set with periodic boundary conditions. In order to avoid additional errors, initial average values in computational domain are assigned by five-order accuracy Gauss integral formula. We compute the solution up to $t = 2.0$. L_1 and L_2 norm errors of density by different methods are shown in Fig. 4, and the orders of accuracy are shown in Table 1. VRM denotes Frink's vertex reconstruction method; LS-2nd and LS-3rd denote second- and third-order K-exact reconstruction methods based on polynomial least squares; RBF-2nd and RBF-3rd denote second- and third-order RBF reconstruction methods in the present paper.

Through the calculation results, we can draw the following two conclusions. Firstly, RBF method has smaller absolute computational errors compared with the traditional K-exact method with regard to the same order accuracy scheme. For the second-order scheme, from Table 1 we can see, the density absolute errors of RBF method are only half of K-exact method. For the third-order scheme, the order accuracy of RBF method can achieve above 3.5, and the errors are almost one magnitude less than those of K-exact method. Thus, RBF reconstruction method performs higher precision and is more accurate than traditional K-exact method. Secondly, RBF reconstruction method is more flexible. Traditional K-exact method, which reconstructs the high-order distribution of flow variables by Taylor series expansion, is a kind of global fitting method. The number of expanded items of Taylor polynomial strictly matches the accuracy order of interpolation method, which is determined by the number of stencil grids. While, on the other hand, RBF method is a kind of local type fitting method, which has strong adaptability for different reconstruction stencils. The interpolation expression is independent of the number of stencil grids, and the numerical accuracy order will preserve a continuous change instead of mutation. The advantage is also beneficial to the numerical stability of flow-field solving.

For this numerical example, the accuracy of third-order RBF method is tested to above 3.5. The reason is that the reconstruction stencil which we used for the third-order scheme is the twice face neighbor stencil which contains six to ten grids, and two Gauss integral points are selected for interface fluxes computing. All of these treatments make the scheme achieve fourth order at the highest. Considering the errors introduced by boundary conditions, we believe this result is reasonable.

The computational time of different methods on the mesh of $\Delta h = 2/80$ is displayed in Table 2. Frink's vertex reconstruction method is the most efficient, since the construction of gradient for control volume is much simpler than K-exact and RBF methods. However, VRM is a linear reconstruction method and is difficult to extend to high-order scheme. For the second-order scheme, RBF method is just slightly slower than K-exact method. And for the third-order scheme, the computational efficiency of RBF method performs not much lower than K-exact method.

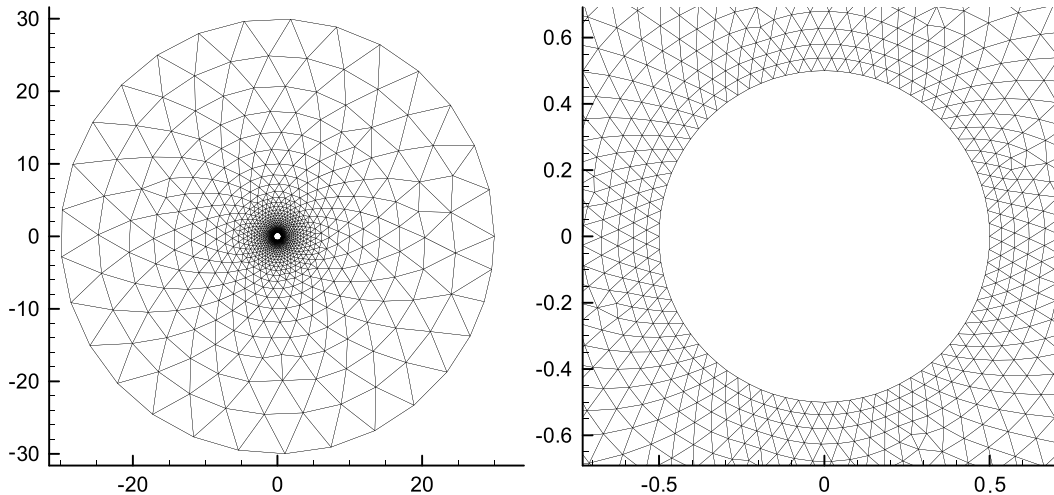
Table 1

Density errors and accuracy order of different reconstruction methods for non-linear Euler equations.

	Mesh	L_1 error	Order	L_2 error	Order
VRM	2/10	3.037E–02		3.394E–02	
	2/20	8.037E–03	1.93	9.094E–03	1.91
	2/40	2.152E–03	1.97	2.495E–03	1.94
	2/80	5.380E–04	1.93	6.557E–04	1.86
LS-2nd	2/10	3.485E–02		3.976E–02	
	2/20	9.655E–03	1.86	1.093E–02	1.87
	2/40	2.575E–03	1.98	2.955E–03	1.96
	2/80	6.209E–04	1.98	7.331E–04	1.94
RBF-2nd	2/10	1.369E–02		1.599E–02	
	2/20	3.362E–03	2.04	3.864E–03	2.06
	2/40	8.263E–04	2.10	9.425E–04	2.11
	2/80	1.884E–04	2.05	2.130E–04	2.07
LS-3rd	2/10	1.029E–02		1.155E–02	
	2/20	1.449E–03	2.84	1.621E–03	2.85
	2/40	1.982E–04	2.98	2.203E–04	2.99
	2/80	2.291E–05	3.00	2.548E–05	3.00
RBF-3rd	2/10	1.598E–03		2.443E–03	
	2/20	1.285E–04	3.65	2.059E–04	3.59
	2/40	1.051E–05	3.75	2.005E–05	3.49
	2/80	6.681E–07	3.83	1.569E–06	3.54

Table 2Comparison of time consumption for different methods on the mesh of $\Delta h = 2/80$.

	VRM	LS-2	RBF-2	LS-3	RBF-3
Time (s)	52.0	77.5	80.3	100.5	121.2

**Fig. 5.** Mesh of the inviscid flow past a circular cylinder.

4.2. Inviscid flow past a circular cylinder

Inviscid flow past a circular cylinder has analytical solution in fluid mechanics, which is usually used as a test case to verify the accuracy of curved boundary conditions for high order schemes. The free stream Mach number is 0.1 and the computational domain is divided into 3228 triangular grids and 80 points on the cylinder surface. The grids of computational domain and the grids near the cylinder surface are shown in Fig. 5.

Numerical solutions to this flow are computed by second- and third-order RBF reconstruction methods, and the second-order method uses straight wall boundary conditions while curved boundary conditions are for the third-order method. Fig. 6(a) shows the pressure isolines and pressure coefficients on the cylinder. We know that the analytical solution of pressure coefficients for this problem is $C_p = 1 - 4 \sin^2 \theta$, where C_p varies from 1.0 at the front stagnation points to -3.0 at the points of maximum velocity and returns to 1.0 at the back stagnation points. And considering Prandtl–Glauert compressibility correction, the analytical pressure coefficients can be slightly larger than the incompressible solution.

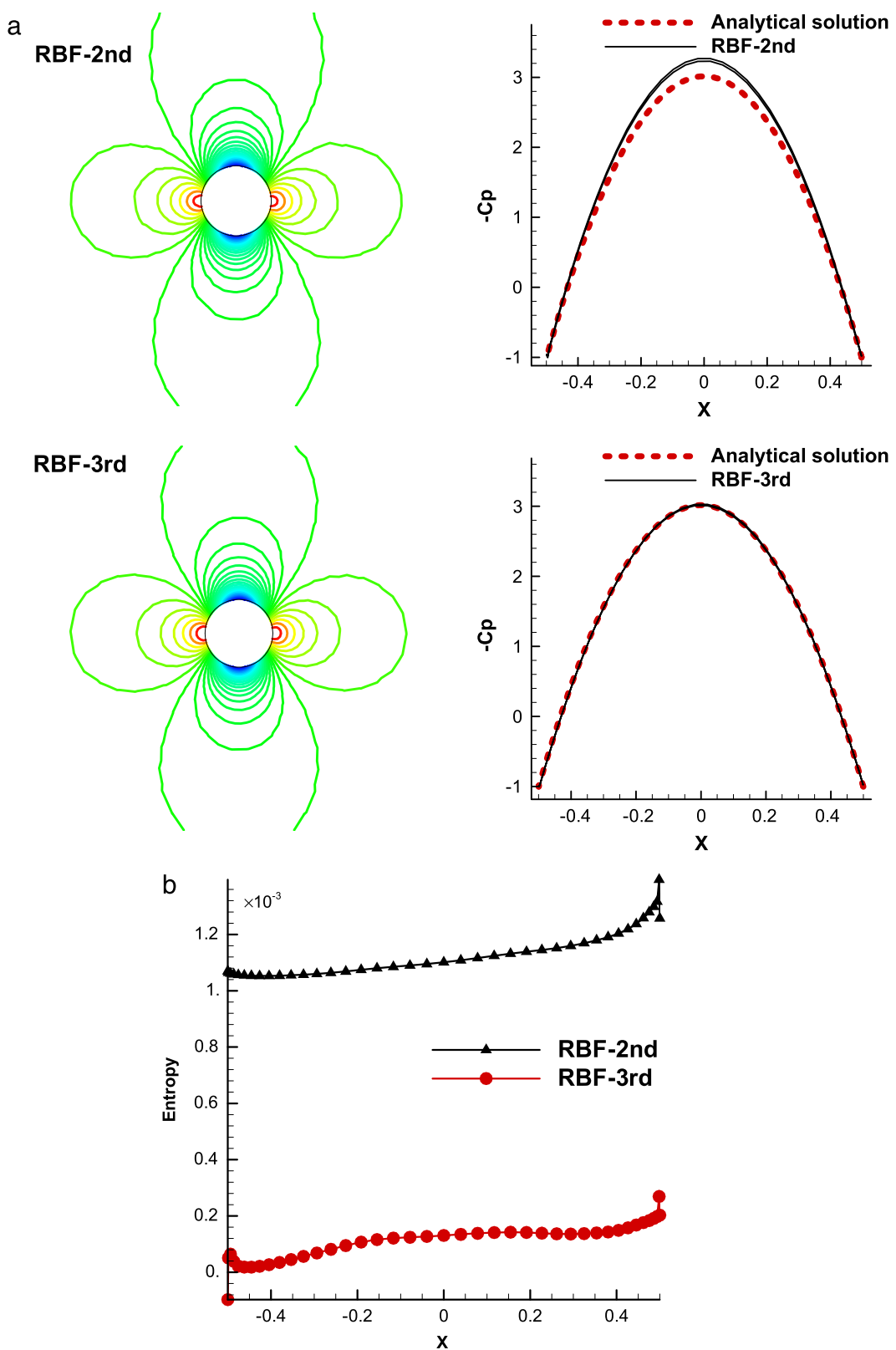


Fig. 6. Computed pressure isolines, pressure coefficients and the entropy production around the circular cylinder by second- and third-order RBF methods. The red dashed line in the pressure coefficients denotes the analytical solution. (For interpretation of the references to color in this figure legend, the reader is referred to the web version of this article.)

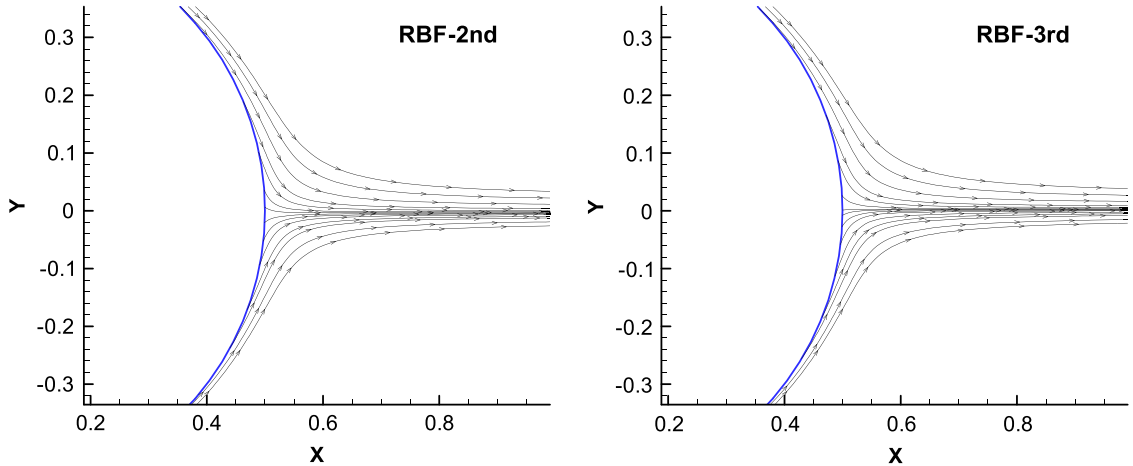


Fig. 7. Streamline patterns near the back stagnation point obtained by the second- and third-order RBF methods.

The entire flow field is symmetrical about both horizontal and vertical axes through the center of the cylinder. From the computational results, for the second-order RBF method, the pressure coefficients are precise enough at both stagnation points; while near the maximum velocity points, the pressure coefficients are a little bigger in computation than in the analytical solution. For the third-order RBF method, as we can clearly see from Fig. 6(a), the entire flow field pressure distribution and the pressure coefficients on the cylinder are both symmetrical about x and y axes. The pressure coefficients over the top of the cylinder match exactly with the bottom, and the results quite coincide with the analytical solution. We further investigate the entropy production on the surface of the cylinder for the second- and third-order RBF methods in Fig. 6(b). The entropy is defined as

$$\varepsilon_{ent} = \frac{P/P_\infty}{(\rho/\rho_\infty)^\gamma} - 1. \quad (24)$$

We know that, for this case, the analytical entropy is zero all around the surface of the cylinder, and the computational result shows that both second- and third-order RBF methods have a small entropy production on the cylinder. The entropy increases slowly from the leading edge to the trailing edge, and also, the third-order RBF method evidently achieves more accurate results than the second-order RBF method does.

Fig. 7 shows the streamlines near the back stagnation point, which are computed by the second- and third-order RBF methods. The streamlines of both methods are clinging and smoothly flowing over the cylinder surface, and there is no unphysical shedding vortex behind the cylinder.

In order to observe the influence of straight boundary conditions on high-order finite volume method, we compute this case by third-order RBF reconstruction method with the straight wall boundary conditions rather than the curved one. Fig. 8 shows the results of pressure coefficients and streamline patterns near the back stagnation point. From the results, there is also no nonphysical vortex exhibited behind the cylinder, while the symmetry of pressure distribution is not as accurate as third-order RBF method with curved boundary conditions. Thus, simply observing this example, the high-order finite volume method based on RBF reconstruction is not as sensitive to straight boundary conditions representation as the discontinuous Galerkin method which may cause false results [43,47]. This opinion is also illustrated in reference paper [48].

4.3. Inviscid isentropic vortex flow

Inviscid isentropic flow [49] is a typical flow to test the resolution of numerical methods. For the Euler equations in two-dimension: the mean flow is $\rho_\infty = 1$, $u_\infty = v_\infty = 1$, $p_\infty = 1$. As an initial condition, an isentropic vortex with no perturbation in entropy is added to the mean flow field. The perturbation values of velocity and temperature are given by

$$(\delta u, \delta v) = \frac{\varepsilon}{2\pi} e^{\frac{(1-r^2)}{2}} (-\bar{y}, \bar{x}) \quad (25)$$

$$\delta T = -\frac{(\gamma - 1)\varepsilon^2}{8\gamma\pi^2} e^{1-r^2}, \quad \delta S = 0 \quad (26)$$

where ε is the vortex strength and $\gamma = 1.4$. Here $T = \frac{p}{\rho}$, $T_\infty = 1.0$ and $r = \sqrt{\bar{x}^2 + \bar{y}^2}$, where $(\bar{x}, \bar{y}) = (x - x_0, y - y_0)$. The initial location of the vortex center is $(x_0, y_0) = (5, 5)$, and the vortex strength $\varepsilon = 5$.

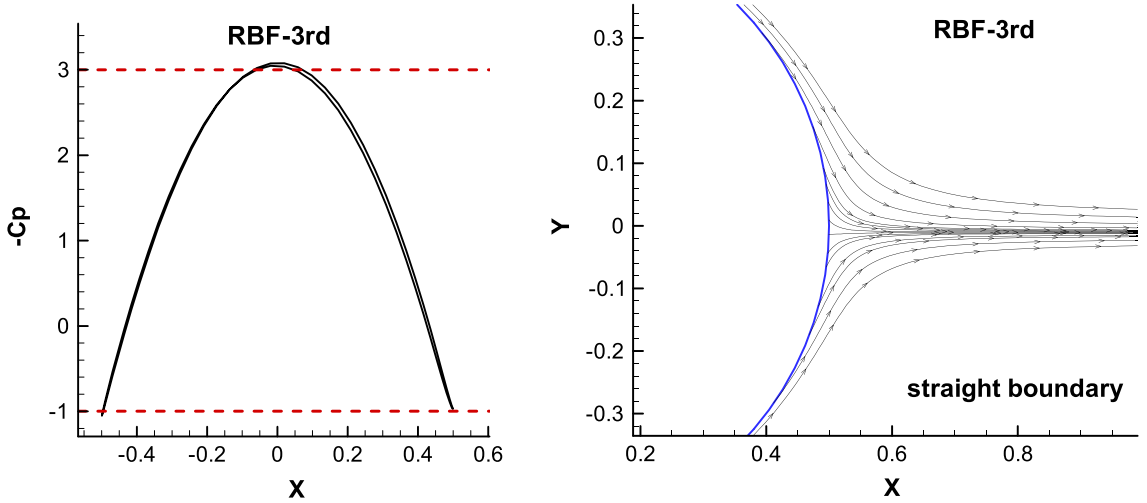


Fig. 8. Pressure coefficients and streamline pattern near the back stagnation point computed by third-order RBF reconstruction method with straight wall boundary conditions for inviscid flow past a circular cylinder.

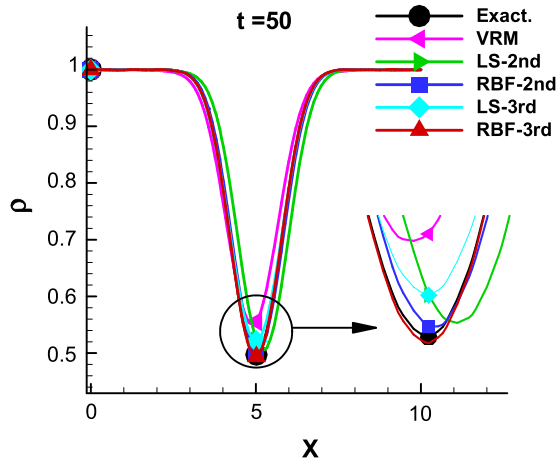


Fig. 9. Density distribution along x -axis at $t = 50$ of different reconstruction methods for inviscid vortex flow.

Thus, the initial values of unsteady flow field are the sum of mean values and perturbation values: $\rho = \rho_\infty + \delta\rho$, $u = u_\infty + \delta u$, $v = v_\infty + \delta v$, $T = T_\infty + \delta T$. And according to the isentropic relation, the resulting state of conservative variables is given by

$$\rho = T^{1/(\gamma-1)} = (T_\infty + \delta T)^{1/(\gamma-1)} = \left[1 - \frac{(\gamma-1)\varepsilon^2}{8\gamma\pi^2} e^{1-r^2} \right]^{1/(\gamma-1)} \quad (27)$$

$$p = \rho^\gamma. \quad (28)$$

The computational domain is $(x, y) \in [0, 10] \times [0, 10]$, and both directions are set with periodic boundary conditions. We use the unstructured grids of the scale $\Delta h = 10/80$. Initial average values in computational domain are assigned the same as those in Section 4.1.

Figs. 9 and 10 are the comparison of density distribution along x -axis at $t = 50$ and $t = 100$ calculated by different reconstruction methods respectively. From the results, we can see, with the increase of time, the density in vortex center rises gradually for the dissipation of numerical schemes. For the second-order methods, the large dissipation and dispersion make the density of vortex center rise up quickly, and the moving locations of vortex center also deviate from the mesh diagonal line. The results of second-order RBF reconstruction method are better than those of the second-order K-exact reconstruction method. In addition, for the third-order scheme, the quality of dissipation and dispersion improves noticeably, and both the density value and the location of vortex center change little compared with the second-order schemes.

In order to make a clear comparison, we compute the long time evolution of the vortex at $t = 10$, $t = 50$, $t = 100$ and $t = 200$, respectively. The results of density along x -axis for second- and third-order schemes are shown in Fig. 11.

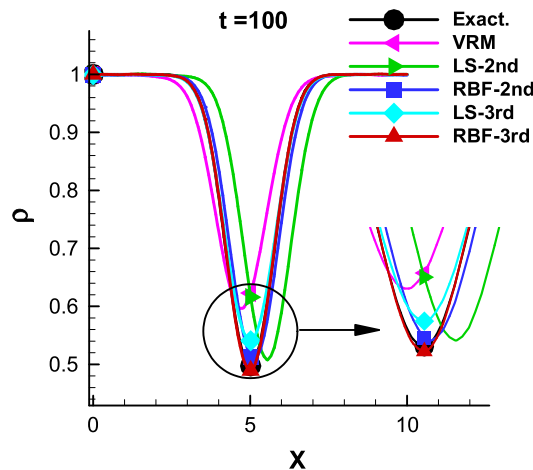


Fig. 10. Density distribution along x -axis at $t = 100$ of different reconstruction methods for inviscid vortex flow.

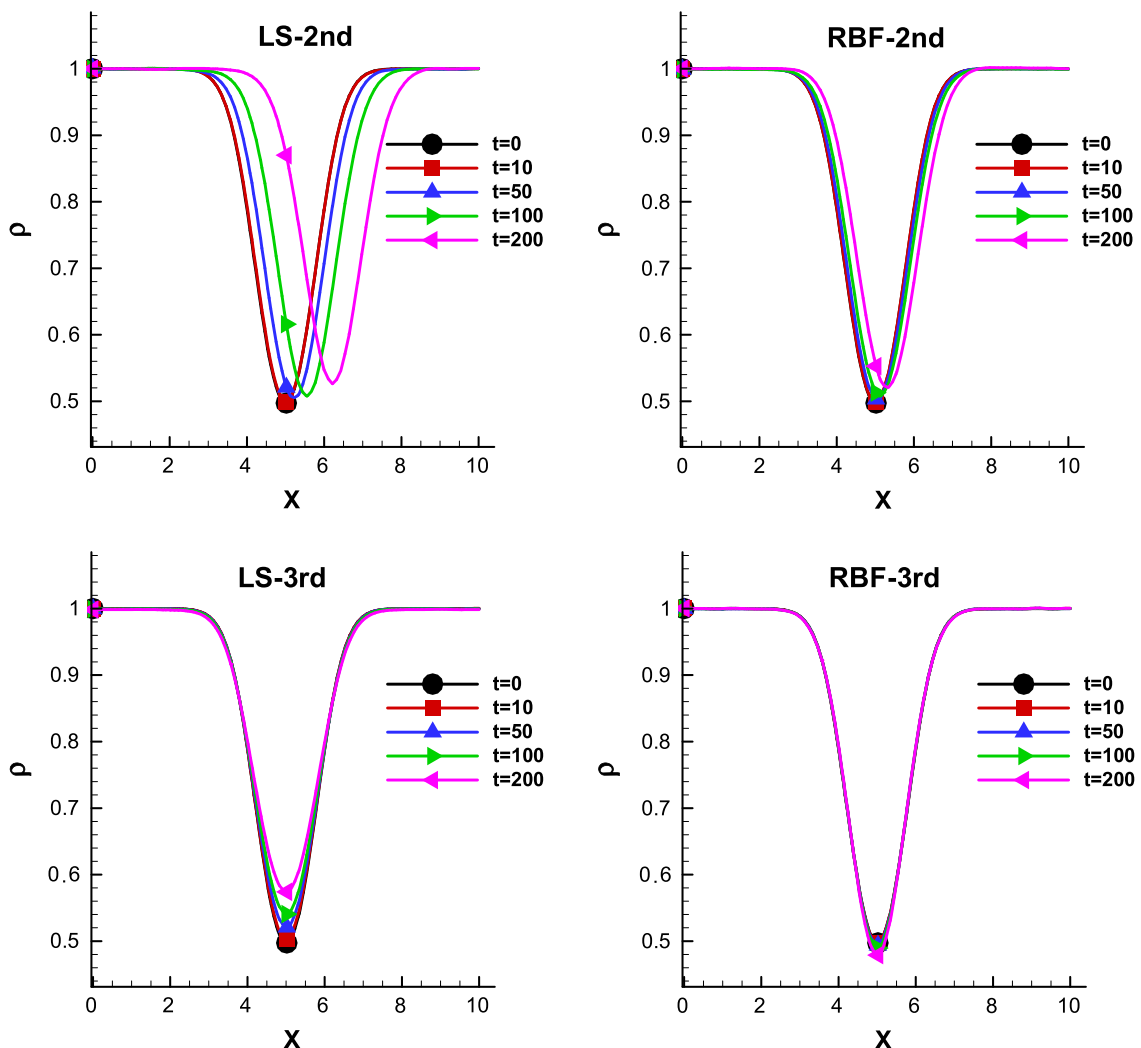


Fig. 11. Density distribution along x -axis at $t = 10, t = 50, t = 100$ and $t = 200$ computed by second-, third-order K-exact and RBF reconstruction methods for inviscid vortex flow.

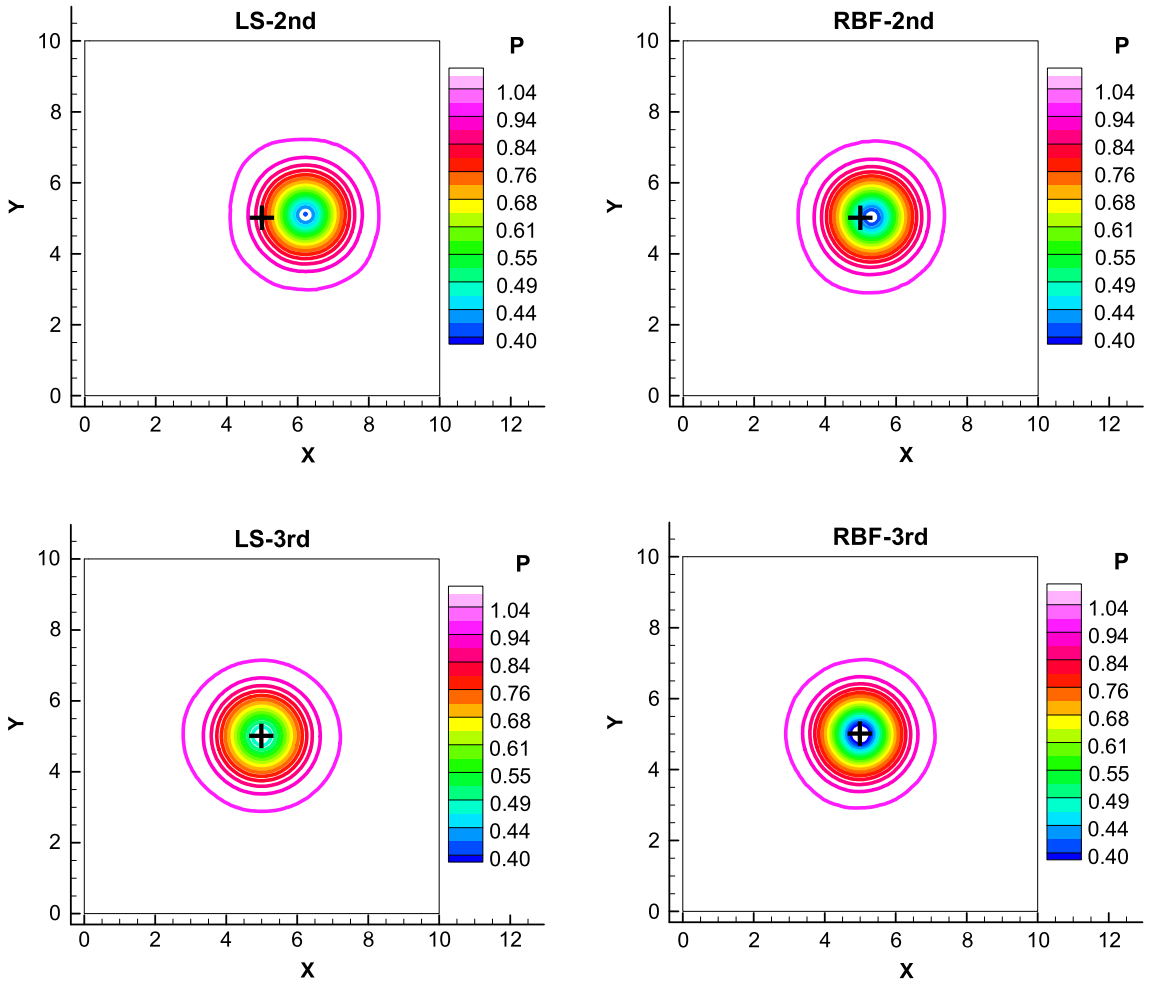


Fig. 12. The location and shape of the vortex at $t = 200$ computed by second-, third-order K-exact and RBF reconstruction methods for inviscid vortex flow.

Compared with the above results, high-order RBF method has lower numerical dissipation. At $t = 10$, the free vortex moves back to the initial location at the first time, and all of the methods present small dissipation and the density distributions vary little compared with initial result. However, as time increases, the dissipation and dispersion of the second-order accuracy scheme increase quickly, and the density value and location of vortex center are obviously different from those of the exact solutions. For the third-order scheme, the location of vertex center remains almost unchanged of both K-exact and RBF methods. For the density of vortex center, RBF method is much more precise than K-exact method. As we can see, the third-order RBF method gives almost no dissipation after 20 motion periods, which shows a much better resolution in flow-field solution.

Fig. 12 displays the shape and position of the free vortex at $t = 200$ for second- and third-order methods with the same contour level of pressure, where the symbol “+” shows the initial position of the vortex. It obviously indicates that the high-order RBF method guarantees more precision results.

4.4. Laminar flow past a stationary circular cylinder

For the vortex-dominated flows, such as helicopter blade vortex interaction and flow over high-lift configurations, there are still many flow problems considered out of reach. Unsteady propagating vortices are the main features of these flow problems, while the second-order methods are too dissipative to elaborately simulate the separation vortex [3].

This section computes the laminar flow past a stationary circular cylinder to simulate shedding vortex by high-order scheme. The free stream Mach number is $M_\infty = 0.1$ and the Reynolds number is $\text{Re} = 100$. The computational domain is divided by 29 788 triangular grids and 100 points on the cylinder surface. In order to test the dissipation of the scheme, we extend the computational domain behind the cylinder to eighty times of the cylinder diameter. The mesh of computational domain is shown in Fig. 13.

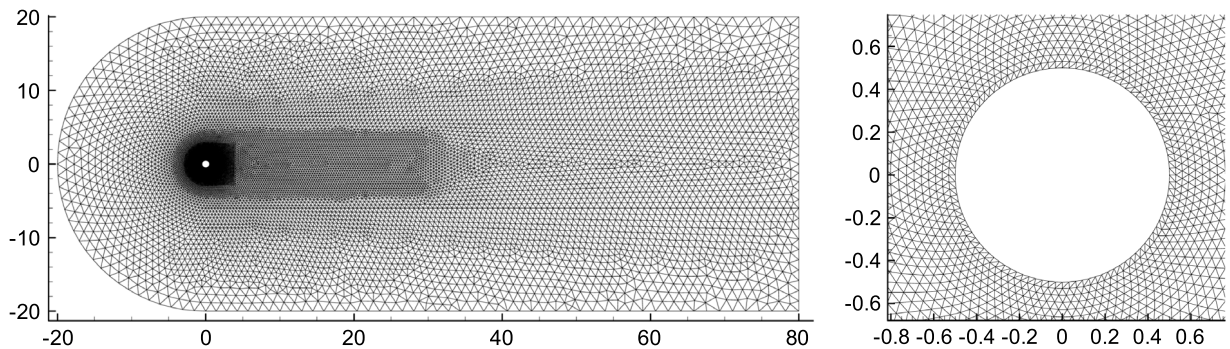


Fig. 13. Mesh of laminar flow past a stationary circular cylinder.

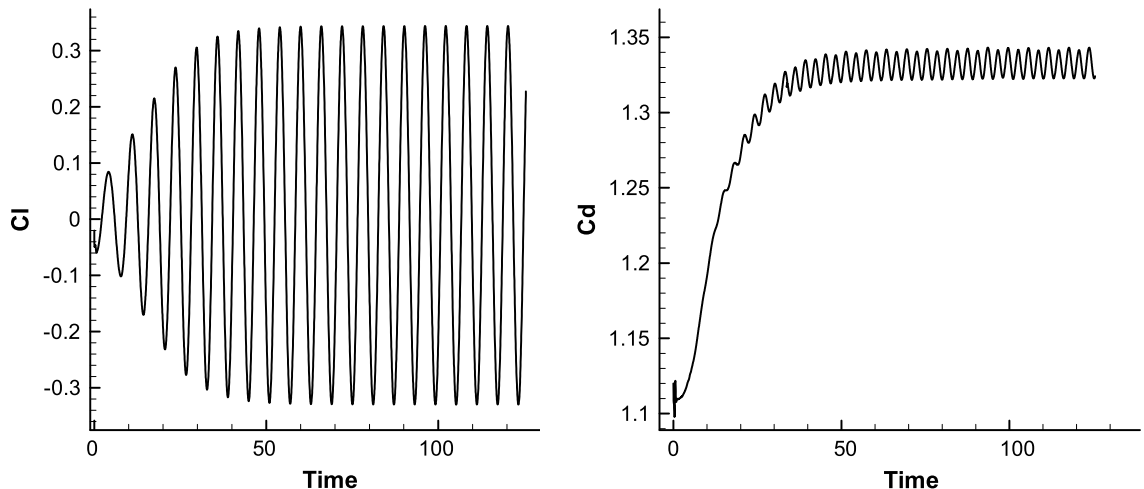


Fig. 14. The lift and drag coefficients responses of the cylinder calculated by third-order RBF reconstruction method for laminar flow past a stationary cylinder.

Table 3

Comparison of amplitude of lift, drag coefficients and Strouhal number (St) with experimental and other reference data, and the computational time for the third-order LS method and RBF method for laminar flow past a stationary cylinder.

	Cl	Cd	St	Time (h)
Tritton [50](exp)	–	1.26	0.160	–
Lu L [51]	0.34	1.35	0.165	–
Baranyi [52]	0.32	1.34	0.164	–
Mingde Su [53]	0.40	1.37	0.163	–
LS-3rd	0.339	1.345	0.166	6.4
RBF-3rd	0.344	1.331	0.166	8.2

Fig. 14 shows the lift and drag coefficients responses of the cylinder by third-order RBF reconstruction method. **Table 3** displays the comparison of amplitudes of lift, drag coefficients and Strouhal number with experimental and other reference data, and the computational time for third-order LS method and RBF method is also shown in **Table 3**. The third-order scheme based on RBF reconstruction method presents a good agreement with the data given in the published literatures, and the computational efficiency of RBF method is a little lower than LS method.

We know that the propagating distance of shedding vortex is determined by the numerical dissipation of calculation schemes. In order to make a clearer comparison, we compute the vorticity distributions of flow field on the same mesh with different reconstruction methods. **Fig. 15** displays 30 isolines with the same levels of flow-field vorticity calculated by the second-, third-order K-exact and RBF methods. The results illustrate that the shedding vortex vanishes at the distance about fifty-five times of the cylinder diameter for the second-order K-exact scheme, while the distance is a little far away computed by the second-order RBF scheme. By contrast, the vortex can nearly maintain for the full flow field by third-order schemes. Compared with K-exact method, the third-order RBF method has smaller numerical dissipation, which is superior in preserving the vortex street behind the cylinder and performs clear and more elaborate vortex structures.

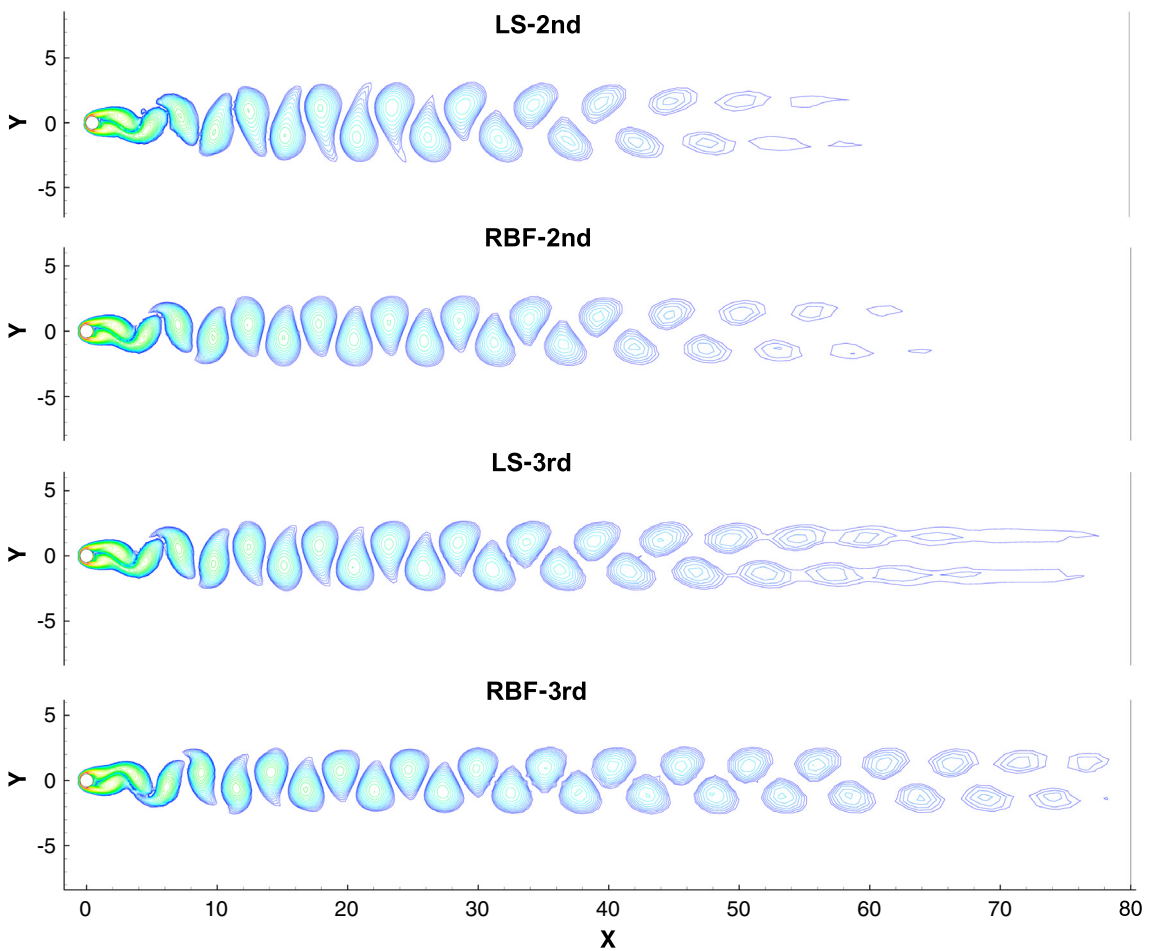


Fig. 15. Vorticity of flow field behind the cylinder computed by K-exact and RBF reconstruction methods for laminar flow past a circular cylinder.

4.5. Viscous flow past a NACA0012 airfoil

In this test, we consider a subsonic laminar flow past the NACA0012 airfoil at an angle of attack $\alpha = 0^\circ$, free stream Mach number $M_\infty = 0.5$, and the Reynolds number $Re_\infty = 5000$. This is a widely used validation case for viscous flow solvers [48,54–57]. The flow separates near the trailing edge and induces a small recirculation region which extends in the wake that is difficult to reproduce accurately. The unstructured hybrid mesh employed for this calculation is depicted in Fig. 16. It contains 22 154 elements and 400 cells are distributed on the surface of the airfoil. The outer boundary is 20 chords far away from the airfoil.

Fig. 17(a) shows the contours of Mach number computed using the third-order RBF scheme, and the pattern of flow separation near the trailing edge and the recirculation zone depicted by flow-field streamlines are shown in Fig. 17(b). We can see clearly that the separation region of the flow occurring near the trailing edge causes the formation of a small recirculation bubble that extends in the near-wake region of the airfoil.

Fig. 18 shows the distribution of the pressure coefficient and the skin friction coefficient over the airfoil surface. The second- and third-order RBF methods precisely coincide with the fourth-order spectral volume approach calculated by Ref. [57]. The separation point computed by third-order scheme is located slightly forward compared with the one of the second-order scheme.

Table 4 gives a comparison of the accuracy of solution as measured by the computed values of pressure drag, viscous drag coefficients and separation point location with values produced by other references. The drag coefficients and the separation point match well with the values in the literature.

5. Conclusions

This paper developed second- and third-order finite volume methods based on RBF reconstruction for the solution to the Euler and Navier–Stokes equations on unstructured grids. The numerical orders are verified by the case of non-linear

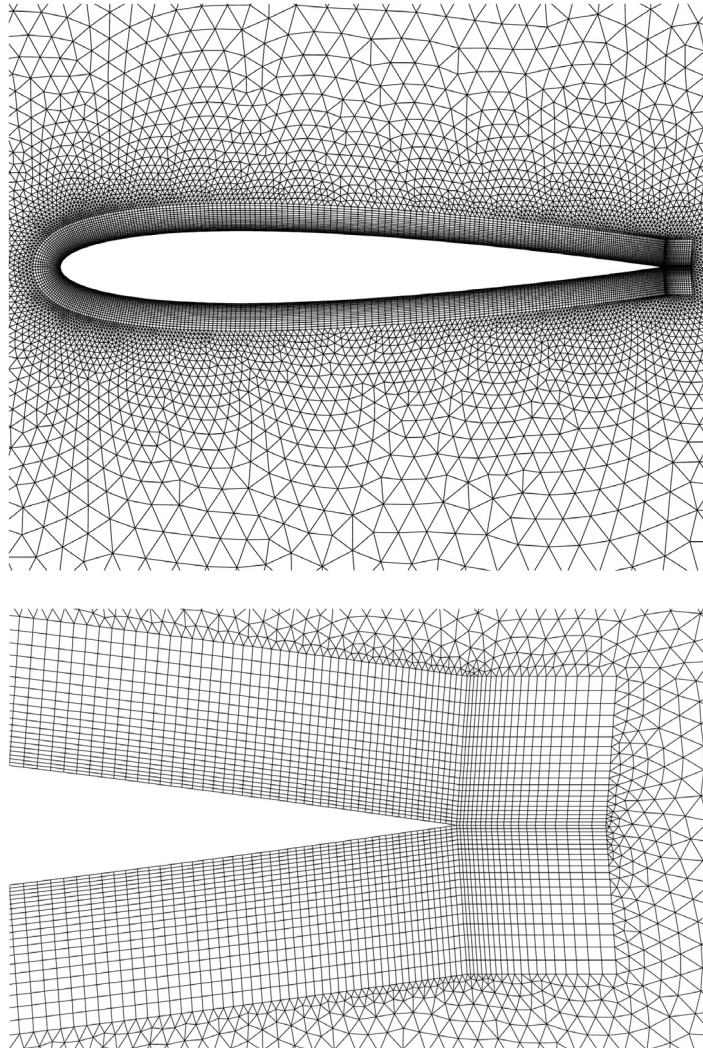


Fig. 16. Computational mesh for viscous flow over the NACA0012 airfoil.

Table 4

Comparison of the drag coefficient and the location of the separation point between the FV-RBF method and previous numerical results for a laminar flow around a NACA0012 airfoil for $M_\infty = 0.5$ and $Re_\infty = 5000$.

	C_d (viscosity)	C_d (pressure)	Separation point
Mavriplis [56]	0.0336	0.0228	0.824
Jawahar [54]	0.0335	0.0226	–
Chassaing (MLS-2nd) [48]	0.0318	0.0222	0.803
Chassaing (MLS-3rd) [48]	0.0328	0.0227	0.808
RBF-2nd	0.0345	0.0243	0.831
RBF-3rd	0.0340	0.0241	0.817

Euler equations. Within the same mesh scale, RBF reconstruction method has better flexibility and smaller absolute errors compared with traditional K-exact scheme. Furthermore, we apply the RBF method to solve several typical flow fields. By inviscid flow past a cylinder, it illustrates the influence of straight and curved boundary conditions on computational results. The high-order RBF finite volume method is not very sensitive to the curved wall boundary conditions. Representation of straight wall boundary will not cause fatal errors but will only reduce the calculation accuracy. The examples of inviscid isentropic vortex, laminar flow past a stationary cylinder and the viscous flow past a NACA0012 airfoil also elaborate that high-order RBF reconstruction method has small numerical errors, low dissipation and high precision. Due to the remarkable advantages of RBF reconstruction method, we think that it will effectively improve the properties of high-order finite volume method.

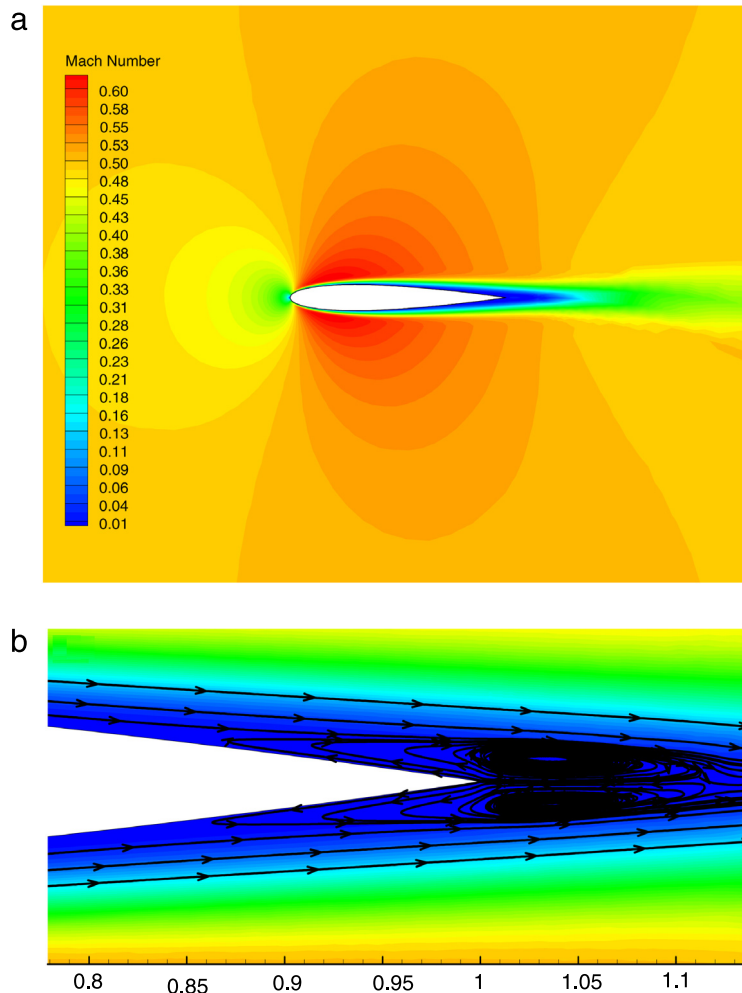


Fig. 17. (a) Contours of the Mach number near the NACA0012 airfoil for $M_\infty = 0.5$ and $Re_\infty = 5000$ obtained by the third-order RBF scheme. (b) Closed view of the small circulation bubble in the near wake.

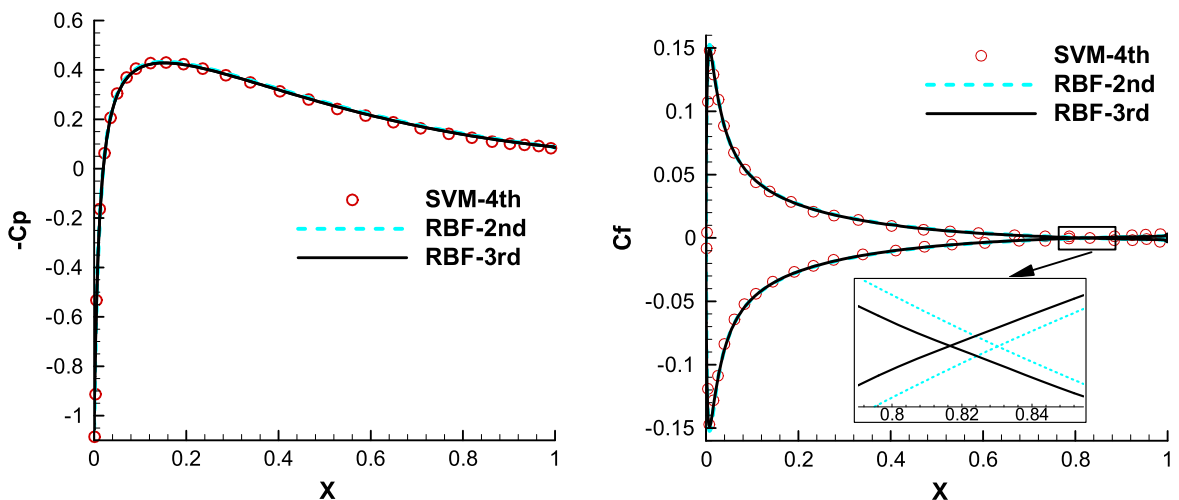


Fig. 18. Comparison of the computed pressure coefficient and the skin friction coefficient over the NACA0012 airfoil surface using the second- and third-order RBF schemes with a fourth-order spectral volume method [57] for $M_\infty = 0.5$ and $Re_\infty = 5000$.

Acknowledgments

The work was supported by the National Natural Science Foundation of China (No. 11172237) and Program for New Century Excellent Talents in University (No. NCET-13-0478). The authors also would like to express gratitude to Professor Yu-Xin Ren in Tsinghua University for the constructive suggestions.

Appendix. Theoretical analysis of the accuracy of RBF interpolation method using MQ basis function in one-dimensional problem

For the equidistance interpolation of three-points in one-dimensional problem, the coordinates of the three base points are $P_1 : (-\Delta x, y_1)$, $P_2 : (0, y_2)$ and $P_3 : (\Delta x, y_3)$. We derive the interpolation function by using polynomial interpolation method and RBF interpolation method respectively.

(1) Polynomial interpolation method based on Taylor series expansion. We assume that the interpolation function can be expressed by quadratic polynomial $f(x) = a_0x^2 + a_1x + a_2$, which is required to satisfy the interpolation conditions

$$\begin{cases} f(-\Delta x) = y_1 \\ f(0) = y_2 \\ f(\Delta x) = y_3 \end{cases} \quad (A.1)$$

Then we can obtain a system of linear equations

$$\begin{bmatrix} \Delta x^2 & -\Delta x & 1 \\ 0 & 0 & 1 \\ \Delta x^2 & \Delta x & 1 \end{bmatrix} \begin{bmatrix} a_0 \\ a_1 \\ a_2 \end{bmatrix} = \begin{bmatrix} y_1 \\ y_2 \\ y_3 \end{bmatrix}. \quad (A.2)$$

The coefficients a_0 , a_1 and a_2 can be determined by solving Eq. (2)

$$\begin{cases} a_0 = \frac{y_1 + y_3 - 2y_2}{2\Delta x^2} \\ a_1 = \frac{y_3 - y_1}{2\Delta x} \\ a_2 = y_2 \end{cases} \quad (A.3)$$

(2) RBF interpolation method. The interpolation function for RBF method can be expressed by

$$f(x) = a_0\varphi_1(\|x + \Delta x\|) + a_1\varphi_2(\|x - 0\|) + a_2\varphi_3(\|x - \Delta x\|). \quad (A.4)$$

where φ denotes basis function. We choose the multiquadric (MQ) basis function, that is $\varphi(r) = \sqrt{c + r^2}$, and take it into the RBF interpolation function. We can rewrite Eq. (4) as

$$f(x) = a_0\sqrt{c + (x + \Delta x)^2} + a_1\sqrt{c + (x)^2} + a_2\sqrt{c + (x - \Delta x)^2}. \quad (A.5)$$

Then, introduce the interpolation conditions, and we can also obtain a system of linear equations

$$\begin{bmatrix} \sqrt{c} & \sqrt{c + \Delta x^2} & \sqrt{c + 4\Delta x^2} \\ \sqrt{c + \Delta x^2} & \sqrt{c} & \sqrt{c + \Delta x^2} \\ \sqrt{c + 4\Delta x^2} & \sqrt{c + \Delta x^2} & \sqrt{c} \end{bmatrix} \begin{bmatrix} a_0 \\ a_1 \\ a_2 \end{bmatrix} = \begin{bmatrix} y_1 \\ y_2 \\ y_3 \end{bmatrix}. \quad (A.6)$$

The coefficients a_0 , a_1 and a_2 can be also determined by solving Eq. (6)

$$\begin{cases} a_0 = \frac{m_2^2 - m_1^2}{(m_1 - m_3)(2m_2^2 - m_1^2 - m_1m_3)}y_1 + \frac{m_2}{2m_2^2 - m_1^2 - m_1m_3}y_2 + \frac{m_1m_3 - m_2^2}{(m_1 - m_3)(2m_2^2 - m_1^2 - m_1m_3)}y_3 \\ a_1 = \frac{m_2}{2m_2^2 - m_1^2 - m_1m_3}y_1 + \frac{m_2}{2m_2^2 - m_1^2 - m_1m_3}y_2 + \frac{m_2}{m_1 - m_3}y_3 \\ a_2 = \frac{m_1m_3 - m_2^2}{(m_1 - m_3)(2m_2^2 - m_1^2 - m_1m_3)}y_1 + \frac{m_2}{2m_2^2 - m_1^2 - m_1m_3}y_2 + \frac{m_2^2 - m_1^2}{(m_1 - m_3)(2m_2^2 - m_1^2 - m_1m_3)}y_3 \end{cases} \quad (A.7)$$

where $m_1 = \sqrt{c}$, $m_2 = \sqrt{c + \Delta x^2}$, $m_3 = \sqrt{c + 4\Delta x^2}$. And we define $t = \frac{\Delta x^2}{c}$, therefore m_1 , m_2 and m_3 can be expressed as $m_1 = \sqrt{c}$, $m_2 = m_1\sqrt{1+t}$, $m_3 = m_1\sqrt{1+4t}$.

In the following, we mainly analyse the properties of RBF interpolation function at $x = 0$ compared with the quadratic polynomial interpolation function. The function value automatically satisfies $f(0) = y_2$, and the detailed illustration for the first-order derivative and second-order derivative at $x = 0$ for the RBF function is given below.

(A). Analysis of the first-order derivative:

$$f'(x) = a_0 \cdot \frac{x + \Delta x}{\sqrt{c + (x + \Delta x)^2}} + a_1 \cdot \frac{x}{\sqrt{c + (x)^2}} + a_2 \cdot \frac{x - \Delta x}{\sqrt{c + (x - \Delta x)^2}}. \quad (\text{A.8})$$

Therefore

$$f'(0) = a_0 \cdot \frac{\Delta x}{\sqrt{c + (\Delta x)^2}} + a_2 \cdot \frac{-\Delta x}{\sqrt{c + (\Delta x)^2}} = (a_0 - a_2) \cdot \frac{\Delta x}{\sqrt{c + (\Delta x)^2}}. \quad (\text{A.9})$$

And substitute the value of coefficients a_0, a_2 into Eq. (9)

$$\begin{aligned} f'(0) &= \frac{y_1 - y_3}{m_1 - m_3} \cdot \frac{\Delta x}{\sqrt{c + (\Delta x)^2}} = \frac{y_1 - y_3}{m_1 - m_1\sqrt{1+4t}} \cdot \frac{\Delta x}{m_1\sqrt{1+t}} \\ &= \frac{y_1 - y_3}{(1 - \sqrt{1+4t})\sqrt{1+t}} \cdot \frac{\Delta x}{m_1^2} = \frac{y_1 - y_3}{(1 - \sqrt{1+4t})\sqrt{1+t}} \cdot \frac{t}{\Delta x} \\ &= \frac{2t}{(\sqrt{1+4t} - 1)\sqrt{1+t}} \cdot \frac{y_3 - y_1}{2\Delta x}. \end{aligned} \quad (\text{A.10})$$

We define:

$$g(t) = \frac{2t}{(\sqrt{1+4t} - 1)\sqrt{1+t}} = \frac{1 + \sqrt{1+4t}}{2\sqrt{1+t}}. \quad (\text{A.11})$$

The radical expressions are expanded by Taylor series, namely

$$\sqrt{1+4t} = 1 + 2t - 2t^2 + O(t^3) \quad (\text{A.12})$$

$$\sqrt{1+t} = 1 + \frac{1}{2}t - \frac{1}{8}t^2 + O(t^3). \quad (\text{A.13})$$

And substitute them to Eq. (11)

$$\begin{aligned} g(t) &= \frac{1 + \sqrt{1+4t}}{2\sqrt{1+t}} = \frac{1 + 1 + 2t - 2t^2 + O(t^3)}{2 \times (1 + \frac{1}{2}t - \frac{1}{8}t^2 + O(t^3))} \\ &= \frac{2 + t - \frac{1}{4}t^2 + t + \frac{9}{4}t^2 + O(t^3)}{2 + t - \frac{1}{4}t^2 + O(t^3)} = 1 + O(t). \end{aligned} \quad (\text{A.14})$$

From the above Eq. (14) we can see, $g(t)$ is different from '1' with regard to the first-order small quantity of 't'. When the value of 't' approaches to zero, that is $\frac{\Delta x^2}{c} \rightarrow 0$, then $g(t) \rightarrow 1$ and $f'(0) \rightarrow \frac{y_3 - y_1}{2\Delta x}$. Compared with the value of the first-order derivative for quadratic polynomial interpolation function, $f'(0) = b = \frac{y_3 - y_1}{2\Delta x}$, they coincide with each other exactly.

(B). Analysis of the second-order derivative:

$$f''(x) = a_0 \cdot \frac{c}{[c + (x + \Delta x)^2]^{3/2}} + a_1 \cdot \frac{c}{[c + (x)^2]^{3/2}} + a_2 \cdot \frac{c}{[c + (x - \Delta x)^2]^{3/2}}. \quad (\text{A.15})$$

Therefore

$$f''(0) = a_0 \cdot \frac{c}{(c + \Delta x^2)^{3/2}} + a_1 \cdot \frac{1}{\sqrt{c}} + a_2 \cdot \frac{c}{(c + \Delta x^2)^{3/2}}. \quad (\text{A.16})$$

And substitute the value of coefficients a_0, a_1 and a_2 into Eq. (16), then

$$f''(0) = \frac{(m_1^4 - m_2^4) \cdot y_1 + (m_1^4 - m_2^4) \cdot y_3}{m_1 m_2 (m_1^2 + m_1 m_3 - 2m_2^2)} + \frac{m_2^2 (m_1 + m_3) - 2m_1^3}{m_1 m_2^2 (m_1^2 + m_1 m_3 - 2m_2^2)} \cdot y_2. \quad (\text{A.17})$$

Replace m_2, m_3 with m_1 and t , then Eq. (17) can be rewritten as

$$\begin{aligned} f''(0) &= \frac{(1 - (1+t)^2) \cdot y_1 + (1 - (1+t)^2) \cdot y_3}{m_1^2 (1+t)^{3/2} (1 + \sqrt{1+4t} - 2(1+t))} + \frac{(1+t)(1 + \sqrt{1+4t}) - 2}{m_1^2 (1+t) (1 + \sqrt{1+4t} - 2(1+t))} \cdot y_2 \\ &= \frac{1}{\Delta x^2} \cdot \left[\frac{t(1 - (1+t)^2) \cdot y_1 + t(1 - (1+t)^2) \cdot y_3}{(1+t)^{3/2} (1 + \sqrt{1+4t} - 2(1+t))} + \frac{t(1+t)(1 + \sqrt{1+4t}) - 2t}{(1+t)(1 + \sqrt{1+4t} - 2(1+t))} \cdot y_2 \right]. \end{aligned} \quad (\text{A.18})$$

(B1). Analysis of the coefficients before y_1 and y_3 :

We define $g_1(t)$ as

$$g_1(t) = \frac{t(1 - (1+t)^2)}{(1+t)^{3/2}(1 + \sqrt{1+4t} - 2(1+t))} = \frac{2t^2 + t^3}{(1+t)^{3/2}(2t - \sqrt{1+4t} + 1)}. \quad (\text{A.19})$$

We expand the radical expressions by Taylor series, then

$$\begin{aligned} g_1(t) &= \frac{2t^2 + t^3}{\left(1 + \frac{3}{2}t + \frac{3}{8}t^2 + O(t^3)\right)[2t + 1 - (1 + 2t - 2t^2 + O(t^3))]} \\ &= \frac{2t^2 + t^3}{2t^2 + 3t^3 + O(t^4)} = \frac{2t^2 + 3t^3 - 2t^3}{2t^2 + 3t^3 + O(t^4)} = 1 + O(t^2). \end{aligned} \quad (\text{A.20})$$

$g_1(t)$ is different from '1' with regard to the second-order small quantity of 't'. When the value of 't' approaches to zero, then $g_1(t) \rightarrow 1$ and the coefficients before y_1 and y_3 approach to $\frac{1}{\Delta x^2}$. And the value of the quadratic polynomial interpolation function is also equal to $\frac{1}{\Delta x^2}$.

(B2). Analysis of the coefficients before y_2 :

We define $g_2(t)$ as

$$g_2(t) = \frac{t(1+t)(1 + \sqrt{1+4t}) - 2t}{(1+t)(1 + \sqrt{1+4t} - 2(1+t))} = \frac{-t + t^2 + (t+t^2)\sqrt{1+4t}}{-1 - 3t - 2t^2 + (1+t)\sqrt{1+4t}}. \quad (\text{A.21})$$

Similarly, we expand the radical expressions by Taylor series, then

$$g_2(t) = \frac{4t^2 + O(t^3)}{-2t^2 + O(t^3)} = -2 + O(t^2). \quad (\text{A.22})$$

From Eq. (22) we can see, $g_2(t)$ is different from '-2' with regard to the second-order small quantity of 't'. When the value of 't' approaches to zero, that is $\frac{\Delta x^2}{c} \rightarrow 0$, then $g_2(t) \rightarrow -2$ and the coefficients before y_2 approach to $\frac{-2}{\Delta x^2}$. Compared with the value of the quadratic polynomial interpolation function, they also coincide with each other exactly.

From the above analysis, for the RBF interpolation method with MQ basis function, the interpolation accuracy is closely related to the distance of interpolation points Δx and the shape parameter c . For the equidistance interpolation of three-points in one-dimensional problem, RBF method has local second-order accuracy at least.

References

- [1] X.G. Deng, M.L. Mao, G.H. Tu, et al., High-order and high accurate CFD methods and their applications for complex grid problems, *Commun. Comput. Phys.* 11 (4) (2012) 1081–1102.
- [2] F. Liao, Z.Y. Ye, L.X. Zhang, Extending geometric conservation law to cell-centered finite difference methods on stationary grids, *J. Comput. Phys.* 284 (2015) 419–433.
- [3] Z.J. Wang, High-order methods for the Euler and Navier–Stokes equations on unstructured grids, *Prog. Aerosp. Sci.* 43 (2007) 1–41.
- [4] A. Jameson, Computational Fluid Dynamics, Past, Present and Future, SciTech, Kissimmee, FL, 2015, January 5, 2015.
- [5] D. Caraeni, D.C. Hill, Unstructured-grid third-order finite volume discretization using a multistep quadratic data-reconstruction method, *AIAA J.* 48 (4) (2010) 808–817.
- [6] C. Ollivier-Gooch, A. Nejat, K. Michalak, Obtaining and verifying high-order unstructured finite volume solutions on the Euler equations, *AIAA J.* 47 (9) (2009) 2105–2120.
- [7] T.J. Barth, D.C. Jespersen, The design and application of upwind schemes on unstructured meshes, *AIAA paper* 89-0366, 1989.
- [8] T.J. Barth, A 3-D upwind Euler solver for unstructured meshes, *AIAA paper* 91-1548, 1991.
- [9] N.T. Frink, P. Parikh, S. Pirzadeh, A fast upwind solver for the Euler equations on three-dimensional unstructured meshes, *AIAA paper* 91-0102, 1991.
- [10] T.J. Barth, P.O. Frederickson, Higher order solution of the Euler equations on unstructured grids using quadratic reconstruction, *AIAA paper* 90-0013, 1990.
- [11] R.M. Curtis, W.W. Robert, K-exact reconstruction for the Navier–Stokes equations on arbitrary grids, *AIAA paper* 93-0536, 1993.
- [12] M. Delanaye, Y. Liu, Quadratic reconstruction finite volume schemes on 3D arbitrary unstructured polyhedral grids, *AIAA paper* 99-3259, 1999.
- [13] C.R. Mitchell, R.W. Walters, K-exact reconstruction for the Navier–Stokes equations on arbitrary grids, *AIAA paper* 93-0536, 1993.
- [14] C. Ollivier-Gooch, V.M. Altena, A high-order accurate unstructured mesh finite-volume scheme for the advection–diffusion equation, *J. Comput. Phys.* 181 (2) (2002) 729–752.
- [15] W.A. Li, Y.X. Ren, High order k-exact WENO finite volume schemes for solving gas dynamic Euler equations on unstructured grids, *Internat. J. Numer. Methods Fluids* 70 (6) (2012) 742–763.
- [16] W.A. Li, Y.X. Ren, The multi-dimensional limiters for solving hyperbolic conservation laws on unstructured grids II: Extension to high order finite volume schemes, *J. Comput. Phys.* 231 (2012) 4053–4077.
- [17] P. Lancaster, K. Salkauskas, Surfaces generated by moving least squares methods, *Math. Comp.* 37 (155) (1981) 141–158.
- [18] L. Cueto-Felgueroso, I. Colominas, J. Fe, et al., High-order finite volume schemes on unstructured grids using moving least-squares reconstruction. Application to shallow water dynamics, *Internat. J. Numer. Methods Engrg.* 65 (3) (2006) 295–331.
- [19] L. Cueto-Felgueroso, I. Colominas, X. Nogueira, et al., Finite volume solvers and moving least-squares approximations for the compressible Navier–Stokes equations on unstructured grids, *Comput. Methods Appl. Mech. Engrg.* 196 (45) (2007) 4712–4736.
- [20] X. Nogueira, L. Cueto-Felgueroso, I. Colominas, et al., A new shock-capturing technique based on moving least squares for higher-order numerical schemes on unstructured grids, *Comput. Methods Appl. Mech. Engrg.* 199 (37) (2010) 2544–2558.
- [21] L. Gu, Moving kriging interpolation and element-free Galerkin method, *Internat. J. Numer. Methods Engrg.* 56 (2003) 1–11.
- [22] K. Plengkhom, W. Kanok-Nukulchai, An enhancement of finite element method with moving Kriging shape functions, *Int. J. Comput. Methods* 2 (4) (2005) 451–475.

- [23] T.Q. Bui, T.N. Nguyen, H. Nguyen-Dang, A moving Kriging interpolation-based meshless method for numerical simulation of Kirchhoff plate problems, *Internat. J. Numer. Methods Engrg.* 77 (2009) 1371–1395.
- [24] B.J. Zheng, B.D. Dai, A meshless local moving Kriging method for two-dimensional solids, *Appl. Meth. Comput.* 218 (2011) 563–573.
- [25] T.Q. Bui, M.N. Nguyen, C.Z. Zhang, A moving Kriging interpolation-based element-free Galerkin method for structural dynamic analysis, *Comput. Methods Appl. Mech. Engrg.* 200 (2011) 1354–1366.
- [26] J.C. Chassaing, X. Nogueira, S. Khelladi, Moving kriging reconstruction for high-order finite volume computation of compressible flows, *Comput. Methods Appl. Mech. Engrg.* 253 (2013) 463–478.
- [27] R.L. Hardy, Multiquadric equations of topography and other irregular surfaces, *J. Geophys. Res.* 76 (8) (1971) 1905–1915.
- [28] A. Boer, M.S. Schoot, H.B. Faculty, Mesh deformation based on radial basis function interpolation, *Comput. & Structures* 85 (2007) 784–795.
- [29] G. Wang, H.M. Haris, Z.Y. Ye, Improved point selection method for hybrid-unstructured mesh deformation using radial basis functions, *AIAA J.* 53 (4) (2015) 1016–1025.
- [30] W.W. Zhang, B.B. Wang, Z.Y. Ye, Efficient method for limit cycle flutter analysis by nonlinear aerodynamic reduced-order models, *AIAA J.* 50 (5) (2012) 1019–1028.
- [31] W.W. Zhang, K.J. Chen, Z.Y. Ye, Unsteady aerodynamic reduced-order modeling of an aeroelastic wing using arbitrary mode shapes, *J. Fluids Struct.* 58 (2015) 254–270.
- [32] S. Morigi, F. Sgallari, The partition of unity method for high-order finite volume schemes using radial basis functions reconstruction, *Numer. Math.* 2 (2) (2009) 153–179.
- [33] T.J. Moroney, I.W. Turner, A three-dimensional finite volume method based on radial basis functions for the accurate computational modelling of nonlinear diffusion equations, *J. Comput. Phys.* 225 (2) (2007) 1409–1426.
- [34] D. Stevens, H. Power, M. Lees, et al., The use of PDE centres in the local RBF Hermitian method for 3D convective-diffusion problems, *J. Comput. Phys.* 228 (12) (2009) 4606–4624.
- [35] T. Sonar, Optimal recovery using thin plate splines in finite volume methods for the numerical solution of hyperbolic conservation laws, *IMA J. Numer. Anal.* 16 (4) (1996) 549–581.
- [36] A. Iske, T. Sonar, On the structure of function spaces in optimal recovery of point functionals for ENO-schemes by radial basis functions, *Numer. Math.* 74 (2) (1996) 177–201.
- [37] C. Shu, H. Ding, K.S. Yeo, Local radial basis function-based differential quadrature method and its application to solve two-dimensional incompressible Navier–Stokes equations, *Comput. Methods Appl. Mech. Engrg.* 192 (7) (2003) 941–954.
- [38] P.L. Roe, Approximate Riemann solvers, parameter vectors, and difference schemes, *J. Comput. Phys.* 43 (1981) 357–372.
- [39] D. Stevens, H. Power, A scalable and implicit meshless RBF method for the 3D unsteady nonlinear Richards equation with single and multi-zone domains, *Internat. J. Numer. Methods Engrg.* 85 (2011) 135–163.
- [40] B. Fornberg, C. Piret, On choosing a radial basis function and a shape parameter when solving a convective PDE on a sphere, *J. Comput. Phys.* 227 (2008) 2758–2780.
- [41] E. Larsson, B. Fornberg, Theoretical and computational aspects of multivariate interpolation with increasingly flat radial basis functions, *Comput. Math. Appl.* 49 (2005) 103–130.
- [42] A. Nejat, C. Ollivier-Gooch, A high-order accurate unstructured finite volume Newton-Krylov algorithm for inviscid compressible flows, *J. Comput. Phys.* 227 (2008) 2582–2609.
- [43] L. Krivodonova, M. Berger, High-order accurate implementation of solid wall boundary conditions in curved geometries, *J. Comput. Phys.* 211 (2006) 492–512.
- [44] F. Bassi, S. Rebay, High-order accurate discontinuous finite element solution of the 2D Euler equations, *J. Comput. Phys.* 138 (2) (1997) 251–285.
- [45] A.H.D. Cheng, M.A. Golberg, E.J. Kansa, et al., Exponential convergence and h-c multiquadric collocation method for partial differential equations, *Numer. Methods Partial Differential Equations* 19 (5) (2003) 571–594.
- [46] J. Qiu, C.W. Shu, Hermite WENO schemes and their application as limiters for Runge–Kutta discontinuous Galerkin method II: two-dimensional case, *Comput. Fluids* 34 (2005) 642–663.
- [47] H. Luo, J.D. Baum, R. Löhner, On the computation of steady-state compressible flows using a discontinuous Galerkin method, *Internat. J. Numer. Methods Engrg.* 73 (2008) 597–623.
- [48] J.C. Chassaing, S. Khelladi, X. Nogueira, Accuracy assessment of a high-order moving least squares finite volume method for compressible flows, *Comput. & Fluids* 71 (2013) 41–53.
- [49] C.W. Shu, Essentially non-oscillatory and weighted essentially non-oscillatory schemes for hyperbolic conservation laws, ICASE Report, 97-65, 1997.
- [50] D.J. Tritton, Experiments on the flow past a circular cylinder at low Reynolds numbers, *J. Fluid Mech.* 6 (4) (1959) 547–567.
- [51] L. Lu, J.M. Qin, B. Teng, et al., Numerical investigations of lift suppression by feedback rotary oscillation of circular cylinder at low Reynolds number, *Phys. Fluids* 23 (3) (2011) 033601.
- [52] L. Baranyi, R.I. Lewis, Comparison of a grid-based CFD method and vortex dynamics predictions of low Reynolds number cylinder flows, *Aeronaut. J.* 110 (1103) (2006) 63–71.
- [53] M.D. Su, Q.J. Kang, Large eddy simulation of the turbulence flow around a circular cylinder at sub-critical Reynolds numbers, *J. Mech.* 31 (1) (1999) 100–105.
- [54] P. Jawahar, H. Kamath, A high-resolution procedure for Euler and Navier–Stokes computations on unstructured grids, *J. Comput. Phys.* 164 (1) (2000) 165–203.
- [55] P. Geuzaine, M. Delanaye, J.A. Essers, Computation of high Reynolds number flows with an implicit quadratic reconstruction scheme on unstructured grids, AIAA paper 97-1947, 1997.
- [56] D.J. Mavriplis, A. Jameson, Multigrid solution of the Navier–Stokes equations on triangular meshes, *AIAA J.* 28 (8) (1990) 1415–1425.
- [57] Y.Z. Sun, Z.J. Wang, Y. Liu, Spectral (finite) volume method for conservation laws on unstructured grids VI: Extension to viscous flow, *J. Comput. Phys.* 215 (2006) 41–58.